

# Extensive study of the quality of fission yields from experiment, evaluation and GEF for anti-neutrino studies and applications \*

*K.-H. Schmidt* <sup>†</sup>, *M. Estienne*, *M. Fallot*  
Subatech CNRS/IN2P3-Université de Nantes-IMTA  
4 rue Alfred Kastler, F-44307 Nantes, France

*B. Jurado*  
CENBG CNRS/IN2P3  
Chemin du Solarium, B.P. 120, F-33175 Gradignan, France

*K. Kern*  
201/145 Symonds Street, Eden Terrace  
Auckland 1010, New Zealand

*Ch. Schmitt*  
IPHC CNRS/IN2P3  
23 rue du Loess, B.P. 28, F-67037 Strasbourg, France

September 3, 2020

---

\*Contribution to the IAEA Technical Meeting on Nuclear Data for Anti-neutrino spectra and applications IAEA Headquarters, Vienna, Austria, 23 to 26 April 2019

<sup>†</sup>[schmidt-erzhausen@t-online.de](mailto:schmidt-erzhausen@t-online.de), URL: [www.khschmidts-nuclear-web.eu](http://www.khschmidts-nuclear-web.eu)

# Contents

<b>1</b>	<b>Introduction</b>	<b>6</b>
<b>2</b>	<b>Theory</b>	<b>7</b>
2.1	GEF . . . . .	8
2.1.1	Concept . . . . .	8
2.1.2	Strengths and weaknesses . . . . .	10
2.1.3	Parameter values . . . . .	11
<b>3</b>	<b>GEF improvements using reactor anti-neutrinos and application to anti-neutrino production</b>	<b>13</b>
3.1	Summation calculations for anti-neutrinos . . . . .	13
3.2	Sensitivity of anti-neutrino spectra to the fission yields . . . . .	14
3.3	Beta-decay emitters . . . . .	16
<b>4</b>	<b>Experimental approaches</b>	<b>21</b>
4.1	Radio-chemistry . . . . .	21
4.1.1	The method . . . . .	21
4.1.2	Independent and cumulative yields . . . . .	21
4.1.3	Yields of short-lived fragments . . . . .	22
4.1.4	Strengths and weaknesses . . . . .	22
4.2	Experiments with particle detectors in direct kinematics . . . . .	23
4.2.1	The method . . . . .	23
4.2.2	Strengths and weaknesses . . . . .	23
4.3	Experiments with particle detectors in inverse kinematics . . . . .	23
4.3.1	The method . . . . .	23
4.3.2	Strengths and weaknesses . . . . .	24
<b>5</b>	<b>Evaluations</b>	<b>24</b>
<b>6</b>	<b>Comparative study</b>	<b>24</b>
6.1	Overall impression . . . . .	24
6.1.1	Illustrative cases . . . . .	25
6.1.2	Treatment of energy distributions: the case of $^{238}\text{U}(n_{fast},f)$ . . . . .	65
6.2	Problems and proposed solutions . . . . .	74
6.2.1	$A=129$ yield in $^{235}\text{U}(n_{th},f)$ . . . . .	74
6.2.2	Mass yields in $^{227}\text{Th}(n_{th},f)$ . . . . .	75
6.2.3	Mass yields in $^{232}\text{U}(n_{th},f)$ . . . . .	76
6.2.4	Mass yields in $^{236}\text{U}(n_{th},f)$ . . . . .	77
6.2.5	Mass yields in $^{237}\text{Np}(n_{th},f)$ . . . . .	78
6.2.6	Mass yields in $^{241}\text{Pu}(n_{th},f)$ . . . . .	81
6.2.7	Mass yields in $^{251}\text{Cf}(n_{th},f)$ . . . . .	84
6.2.8	Mass yields in $^{254}\text{Es}(n_{th},f)$ . . . . .	86
6.2.9	Mass yields in $^{255}\text{Fm}(n_{th},f)$ . . . . .	87
6.3	Summary . . . . .	88

<b>7</b>	<b>Predictions of anti-neutrino energy spectra based on the GEF fission yields</b>	<b>88</b>
7.1	Anti-neutrino energy spectra . . . . .	89
7.2	Sensitivity to the fissioning system . . . . .	90
<b>8</b>	<b>Conclusion</b>	<b>90</b>

**Abstract:** The understanding of the anti-neutrino production in fission and the theoretical calculation of the anti-neutrino energy spectra in different, also future, types of fission reactors rely on the application of the summation method, where the individual contributions from the different radioactive nuclides that undergo a beta decay are estimated and summed up. The first step of this kind of calculation is the most accurate estimation of the independent fission-fragment yields. This is a complex task, because the yields depend on the fissioning nucleus and on the energy spectrum of the incident neutrons.

In the present contribution, the quality of different sources of information on the fission yields is investigated, and the benefit of a combined analysis is demonstrated.

Fission-fragment yields can be measured with different techniques. The traditional radio-chemical method, which is almost exclusively used for evaluations, provides an un-ambiguous identification in  $Z$  and  $A$ , but it is restricted to a limited number of suitable targets, it is slow, and the accuracy suffers from uncertainties in the spectroscopic nuclear properties. Experiments with powerful spectrometers, for example at LOHENGRIN, provide very accurate mass yields and a  $Z$  resolution for light fragments from thermal-neutron-induced fission of a few suitable target nuclei. The innovative inverse-kinematics approaches provide excellent resolution in  $A$  and  $Z$  of all fission products for a large variety of fissioning systems. Due to some problems, e.g. in the resolution of the induced energy, they have not yet been exploited for evaluations.

On the theoretical side, the general fission model GEF has been developed. It combines a few general theorems, rules and ideas with empirical knowledge. GEF covers almost all fission observables and is able to reproduce measured data with high accuracy while having remarkable predictive power by establishing and exploiting unexpected systematics and hidden regularities in the fission observables. In this article, we have coupled for the first time the GEF predictions for the fission yields to fission-product beta-decay data in a summation calculation of reactor anti-neutrino energy spectra. The first comparisons performed between the spectra obtained with GEF and those obtained with the evaluated nuclear databases exhibited large discrepancies that highlighted the need of additional constraints for the GEF model in order to reach the level of accuracy required by the anti-neutrino energy spectra. The combination of a careful study of the independent isotopic yields and the adjunction of the LOHENGRIN fission-yield data as additional constraints led to a substantially improved agreement between the anti-neutrino spectra computed with GEF and with the evaluated data.

The main results of this study are :

- an improved agreement between the anti-neutrino energy spectra obtained with the newly tuned GEF model and the JEFF 3.1.1 and JEFF 3.3 fission yields for the four main contributors to the fissions in standard power reactors,
- a demonstration of the benefit from cross-checking the results of different experimental approaches and GEF for improving the quality of nuclear data,
- an analysis of the sources of uncertainties and erroneous results from different experimental approaches,

- the capacity of GEF for predicting the fission yields (and other observables) in cases (in terms of fissioning systems and excitation energies) which are presently not accessible to experiment,
- predictions of anti-neutrino energy spectra that aim to assess the prospects for reactor monitoring, based on the GEF fission yields associated with the beta decay data of the most recent summation model.

# 1 Introduction

When a heavy nucleus breaks apart, the two fragments, even after prompt-neutron emission, are usually situated at the neutron-rich side of the nuclear chart. Thus, most of them undergo a sequence of several beta-minus decays, until the beta-stability line is reached. In each beta decay, an anti-neutrino is produced. Each beta emitter is characterised by a specific anti-neutrino spectrum, which is determined by the beta Q value and the relative population of ground and excited states in the respective daughter nucleus. Fission reactors form particularly strong anti-neutrino sources [1], which can be used for particle physics studies [2, 3, 4, 5] or for technical purposes. The total spectrum of all these contributions from all the fissioning species in a fission reactor is characteristic for the operation method of the reactor and was proposed to be exploited for reactor monitoring [6]. Up to recently, integral measurements of the beta spectra [7, 8, 9, 10] of the main fission sources of a power reactor,  $^{235}\text{U}$ ,  $^{239}\text{Pu}$ ,  $^{241}\text{Pu}$  and  $^{238}\text{U}$ , were used to obtain the anti-neutrino emission by the reactor neutrino experiments. In 2011, these converted spectra were computed again and the comparison between the newly obtained predictions and reactor anti-neutrino experiment results showed a 6% discrepancy [11, 12] called the "reactor anomaly". A little later, a shape discrepancy between 5 and 7 MeV in anti-neutrino energy was evidenced between measured anti-neutrino spectra and the same predictions, called the shape anomaly [13]. These unexplained discrepancies triggered numerous studies in several directions: search for sterile neutrinos at reactors [14, 15]; exploration of potential biases of the conversion model [16, 17, 18]; development of an alternative model based on nuclear data i.e. the summation method [11, 19, 20, 21, 22]. The first pre-requisite of a summation calculation of these anti-neutrino spectra is an accurate estimation of the independent fission-fragment yields, that means the yields before beta decay. The crucial importance of this point is demonstrated by the considerably diverging anti-neutrino spectra obtained by using different evaluations [23, 24]. In particular, drastic discrepancies were found in the anti-neutrino spectrum, which amount to more than 30 % around 5 to 6 MeV for  $^{235}\text{U}(n_{th},f)$  when using fission yields from ENDF/B-VII-1, JEFF 3.1.1 and JENDL 4.0, respectively. Also fragments with small yield can have strong influence on the anti-neutrino spectrum, because only few beta emitters may contribute to certain regions in the anti-neutrino spectrum.

In the present contribution, we investigate, how a combined analysis of experiment, evaluation and theory can lead to an improved quality of fission-fragment yield estimations. In particular, we demonstrate the benefit of including a theoretical model in this process. The GEF model [25] seems to us best suited for this purpose. The calculation of anti-neutrino energy spectra with fission yields resulting from different sets of parameters of the GEF model allows tuning these parameters to better reproduce those computed with the JEFF fission yields. In the first part of this article, after a presentation of the GEF model, we present comparisons between anti-neutrino energy spectra built with the GEF and the JEFF fission yields. We explain how it led to improvements of

the model through the adjunction of experimental constraints such as the LO-HENGRIN sets of fission yields. We then show the level of agreement reached between JEFF and GEF on the anti-neutrino energy spectra from a standard power reactor fuel. In a second part of this article, we review the experimental methods available to bring additional experimental constraints to the evaluated fission yields. We then give a general view on a large variety of fissioning systems with the aim to test the validity of the postulated regularities of the GEF model, which are crucial for its predictive power. The comparison is made for all systems, for which empirical fission-fragment yields from evaluations<sup>1</sup> or from selected highly accurate kinematical experiments on thermal-neutron-induced fission are available. In addition, the fast-neutron-induced fission of  $^{238}\text{U}$  is included due to its contribution to the anti-neutrino production in a reactor. This wide overview that includes also many systems, which do not contribute to the anti-neutrino production in currently operated reactors, allows us to obtain a complete picture of the deviations between GEF and the available empirical data and to locate their origin. It is also useful for estimating the anti-neutrino production in future fission reactors with different kinds of fuel. In the last section of this article, we provide predictions of anti-neutrino energy spectra for the corresponding fissioning systems.

## 2 Theory

The fully theoretical (microscopic) description of the complete fission process has not yet attained the accuracy that makes it suitable for technical applications. Only the description of pre-saddle and post-scission phenomena, in particular the fission cross section and the de-excitation of the fission fragments, is well mastered by highly developed and rather sophisticated optical-model and by dedicated statistical de-excitation codes, respectively, while the dynamical evolution of the system between saddle and scission, which is decisive for the fission yields, poses still a severe challenge to theory, see [26].

Therefore, we focus in this contribution on a semi-empirical approach, the general fission model GEF [25], which is based on a number of concepts and laws of general validity. GEF has shown to reproduce measured data remarkably well, and, thus, it is reasonable to expect its predictive power to be most reliable. GEF covers the whole fission process, beginning from the formation of an excited system and ending after the radioactive decay of the fission fragments towards the beta-stable end products. This model has a set of empirical parameters, which are adjusted to the available empirical information. The GEF model with a set of well adjusted parameters is able to predict the fission quantities of other systems with an accuracy comparable with the uncertainties of the experimental data used for the parameter fit [27].

---

<sup>1</sup>In this work, evaluated data are considered as empirical information, because they are essentially based on measured data.

## 2.1 GEF

### 2.1.1 Concept

A detailed description of the GEF model can be found in ref. [25]. Here, we only give a succinct and somewhat simplified description of the main ideas that are specific to the GEF model. The calculations in this work were performed with the latest version GEF-Y2019/V1.2.

Figure 1 shows a flow diagram of the GEF code, which documents the treatment of the different steps of the fission process.

- The GEF code uses the Monte-Carlo approach to generate even-by-event information of nearly all observables.

- Each event starts from a specific, eventually excited and rotating, nucleus as given by the user (spontaneous fission from the nuclear ground state or by specifying the reaction, e.g. neutron or proton bombardment, or by indicating the compound nucleus and its excitation energy and angular momentum directly). GEF calculates the decay of the system by fission in competition with the emission of neutrons, protons and photons. Pre-equilibrium emission is included also whenever suited.

- In case the system is committed to fission, the distributions of the fragment properties at scission ( $A, Z$ , kinetic energies, excitation energies and deformation) are calculated. Then, the de-excitation of the primary fragments is calculated by a competition between neutron, proton and gamma emission, till the cold secondary fragments reach the ground state or an isomeric state. For those products which are radioactive, GEF can compute as well their decay by beta emission, delayed neutrons etc..

- The main ingredients of the GEF code entering the modeling of the fission probability and fragment properties, and which are often specific to GEF, are shortly discussed below. The modeling of particle evaporation and gamma emission, in Weisskopf theory, however with explicit consideration of angular-momentum-dependent nuclear properties, is more standard, and is not mentioned further. Details can be found in [25]

**Fission barriers:** The most important physical property for the modeling of the fission probability is the fission barrier. The fission barriers are calculated by use of the topographic theorem [28] as the sum of the macroscopic barrier and the additional binding energy by the ground-state shell correction. This approach avoids the uncertainties of the theoretical shell-correction energies.

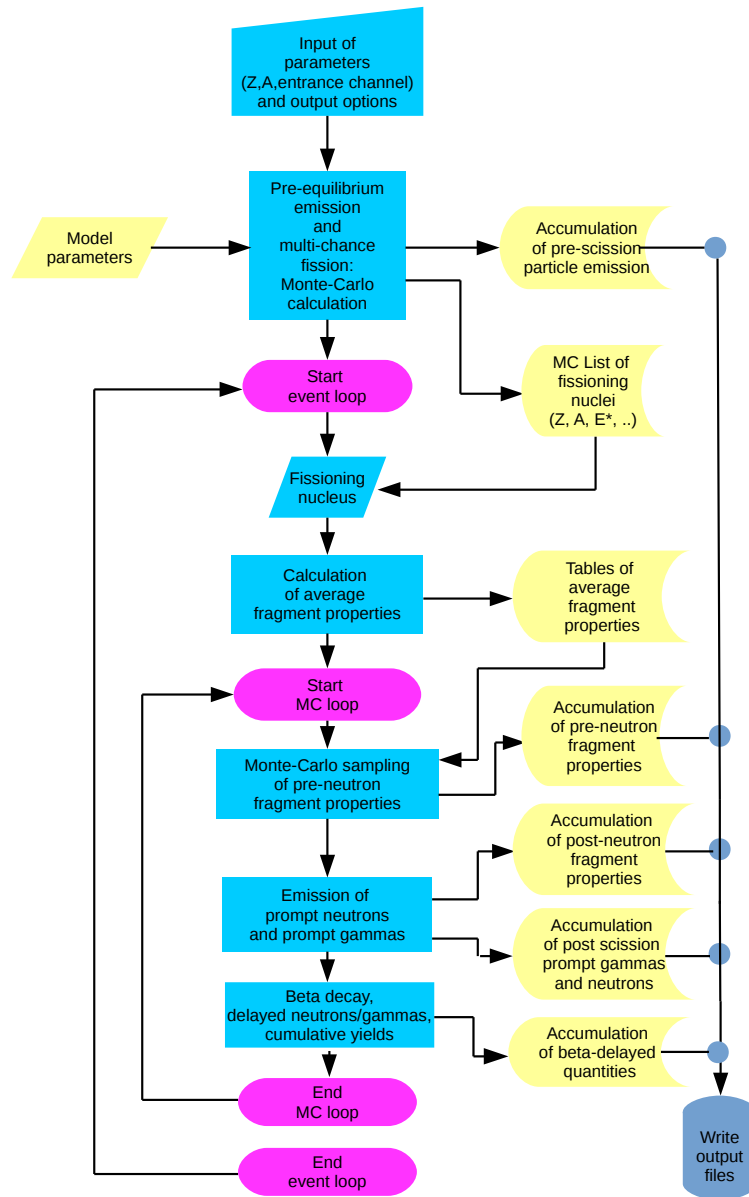


Figure 1: Flow chart of the GEF code.

**Fission channels:** Fission-fragment yields are given by the superposition of the yields associated to different fission channels. The fission channels are related to the statistical population of quantum oscillators in the mass-asymmetry degree of freedom that form the fission valleys in the multidimensional potential-energy landscape. The three parameters (position, depth, and curvature) are traced back to the macroscopic potential (symmetric, 'super-long' fission channel SL) and to shells in the proton and neutron subsystems of both fragments ('standard' fission channels S1 and S2), which are assumed to be effective already at or little behind the outer saddle [29]. The description of the S2 fission channel requires two additional parameter, because its shape is parametrized as a rectangular distribution convoluted with two Gaussian distributions at the inner and the outer side, respectively.

These shells are assumed to be essentially the same for all fissioning systems. Only the superposition of different shells and the interaction with the macroscopic potential cause the different mass distributions found for different systems [30]. These shells also determine the shapes (mainly the quadrupole deformation) of the nascent fragments at scission. According to Strutinsky-type calculations, the fragment shapes are found to be a linearly increasing function of the number of protons, respectively neutrons in regions between closed spherical shells [31]. Also the charge polarization (deviation of the  $N/Z$  degree of freedom at scission - mean value and fluctuations - from the  $N/Z$  value of the fissioning nucleus) is treated by the corresponding quantum oscillator [32].

**Energy sorting:** The excitation energy of the fragments at scission is essential to determine the de-excitation of the fragments via prompt neutron and gamma emission after scission. To infer the excitation energy of the individual fragments at scission, it is necessary to model, how the total available intrinsic excitation energy at scission is shared between the two fragments. In GEF, this is ruled by the so called energy-sorting process. By the influence of pairing correlations, the nuclear temperature below the critical pairing energy is assumed to be constant [33]. Therefore, the di-nuclear system between saddle and scission consists of two coupled microscopic thermostates [34]. This leads to a sorting process of the available intrinsic energy before scission [35, 36], where most of the excitation energy available at scission goes to the heavy fragment. The energy sorting has an important influence on the odd-even effect in the fragment  $Z$  distribution [37] and on the fragment-mass-dependent prompt-neutron multiplicity.

### 2.1.2 Strengths and weaknesses

The GEF model combines a well defined theoretical framework of basic concepts and laws of general validity with the ability to closely reproduce measured fission observables by adjusting the values of the model parameters in a rather direct and flexible way. Thus, it goes well beyond the purely empirical description of systematics without the necessity of a complete and accurate understanding of the physics in an ab-initio approach. The concept of the GEF model combines the strength of an empirical systematics with the strength of a rather

far-reaching understanding of the physics. This leads to a good reproduction of measurements and a good predictive power [25, 27, 26].

Inevitably, the theoretical framework includes some approximations and simplifications. These give rise to a somewhat imprecise representation of the physics that leads to limitations in both the exact reproduction of measured observables and the accuracy of the predictions. Even though, systematic investigations [25] revealed that the accuracy of GEF is often comparable with the uncertainties of the experimental data.

### 2.1.3 Parameter values

The parameter values of the GEF model are very close to the ones documented in ref. [27]. However, a few modifications were recently introduced to better represent the empirical fission yields of the JEFF 3.1.1 and the JEFF 3.3 evaluation as well as the LOHENGRIN experiments, which were not considered before. In particular, the very accurate mass yields of the LOHENGRIN experiments required an individual adjustment, depending on the  $Z$  value of the fissioning nucleus. Still, all isotopes of a given element are described with the same parameter set. The modified parameter values (all related to the modeling of the fission channels) are documented in tables 1. We refer to [25, 27] for their exact meaning.

The strength of the shell effect for symmetric fission has to be determined for individual fissioning systems, because the nuclides formed in symmetric fission depend on the composition of the fissioning nucleus. However, this was only possible in a limited number of cases, where the required experimental information is available. These values are listed in table 2. They vary by a few 100 keV. Such a small difference suggests the high sensitivity of the fragment yield at symmetry to this critical parameter.

Table 1: List of locally adjusted parameter values.

Parameter	Global values	Locally adjusted values	
		$Z = 90$	$Z = 93, 94, 95$
$P\_DZ\_Mean\_S1$	0	(0)	0.25
$P\_DZ\_Mean\_S2$	0	0.6	-0.3
$P\_Shell\_S2$	-4.4 MeV	-4.8 MeV	(-4.4 MeV)
$P\_Z\_Curv\_S2$	0.098	0.25	0.08
$S2leftmod$	0.75	(0.75)	0.65
$P\_A\_Width\_S2$	11.5	12.5	(11.5)

Note: Local values that are identical with the global ones are given in parentheses. Global parameter values are used for all elements with  $Z$  different from 90, 93, 94, and 95.

Explanation of the parameter names:

- $P\_DZ\_Mean\_S1$ : Shift of the S1 fission channel in  $Z$  with respect to the value of the global parameter set.
- $P\_DZ\_Mean\_S2$ : Shift of the S2 fission channel in  $Z$ .
- $P\_Shell\_S2$ : Strength of the shell behind the S2 fission channel.
- $P\_Z\_Curv\_S2$ : This parameter determines the smoothing of the inner side of the potential pocket of the S2 fission channel.
- $S2leftmod$ : This parameter determines the smoothing of the outer side of the potential pocket of the S2 fission channel.
- $P\_A\_width$ : Flat part of the S2 potential pocket.

Table 2: Adapted values of the strength of the shell effect for symmetric fission.

$Z = 89$							
$A =$	226						
$Delta\_S0/MeV =$	-0.3						
$Z = 90$							
$A =$	228	229	230	231	232	233	
$Delta\_S0/MeV =$	0.2	0.4	0.7	0.8	0.9	0.9	
$Z = 92$							
$A =$	233	234	all other				
$Delta\_S0/MeV =$	0.4	0.4	0.2				
$Z \geq 93$							
$A =$	all						
$Delta\_S0/MeV =$	-0.3						

Note: The values are adjusted to the relative yield of the symmetric channel in measured mass distributions. Data from JEFF 3.3 ( $n_{th,f}$ ) and refs. [38, 39] (transfer reactions) were used. For all other cases:  $Delta\_S0 = 0$ . See refs. [25, 27] for the meaning of  $Delta\_S0$ .

### 3 GEF improvements using reactor anti-neutrinos and application to anti-neutrino production

Anti-neutrino energy spectra of individual fission products obtained from nuclear databases have been used to refine the GEF code in order to improve its potential of predictiveness for reactor anti-neutrinos. In the present section, reactor anti-neutrino energy spectra have been computed using summation calculations with decay data taken from nuclear databases and fission yields taken respectively from GEF, JEFF-3.1.1 and JEFF-3.3. The direct comparison of the three calculations allowed us to extensively improve the predictions of GEF for anti, -neutrinos by acting on a few well identified parameters depending on the fission channel concerned.

#### 3.1 Summation calculations for anti-neutrinos

The summation method is based on the use of nuclear data combined in a sum of all the individual contributions of the beta branches of the fission products, weighted by the amount of the latter nuclei. Two types of datasets are thus involved in the calculation: fission product decay data, and fission yields. This method was originally developed by [40] followed by [41] and then by [42, 43]. The  $\beta/\bar{\nu}$  spectrum per fission of a fissible isotope  $S_k(E)$  can be broken-up into the sum of all fission product  $\beta/\bar{\nu}$  spectra weighted by their activity  $A_{fp}$

$$S_k(E) = \sum_{fp=1}^{N_{fp}} A_{fp} \times S_{fp}(E) \quad (1)$$

Eventually, the  $\beta/\bar{\nu}$  spectrum of one fission product is the sum over the  $b$  branches of all  $\beta$  decay spectra (or associated  $\bar{\nu}$  spectra),  $S_{fp}^b$  (in eq 2), of the parent nucleus to the daughter nucleus weighted by their respective branching ratios as

$$S_{fp}(E) = \sum_{b=1}^{N_b} BR_{fp}^b \times S_{fp}^b(Z_{fp}, A_{fp}, E_{0fp}^b, E) \quad (2)$$

In the summation spectra presented in this article, the beta decay properties of the fission products have been selected following the prescription of [22] and include the most recent Total Absorption Gamma-ray Spectroscopy (TAGS) data which are free from the Pandemonium effect [44]. The Pandemonium effect is the main bias of the anti-neutrino energy spectra computed with the summation method, its impact being larger than other nuclear effects such as forbidden non-unique shape factors or the weak magnetism correction. It arises from the use of Germanium detectors to detect the beta branches of beta decays with large Q-value. In some cases, the lack of efficiency of these captors to high energy or multiple gamma-rays induce the mis-detection of beta branches towards high energy states in the daughter nucleus. This leads to the distortion of the beta and anti-neutrino spectra with an over-estimate of the high energy

part. The measurement of beta decay properties with the TAGS technique [45] allows to circumvent the problem, and experimental campaigns focussed on nuclei contributing importantly to the reactor anti-neutrino spectra have been performed in Jyväskylä since 2009 [19, 20, 46, 47, 48, 49], leading to an impressive improvement of the agreement between the summation method predictions and the Daya Bay experimental results [22].

### 3.2 Sensitivity of anti-neutrino spectra to the fission yields

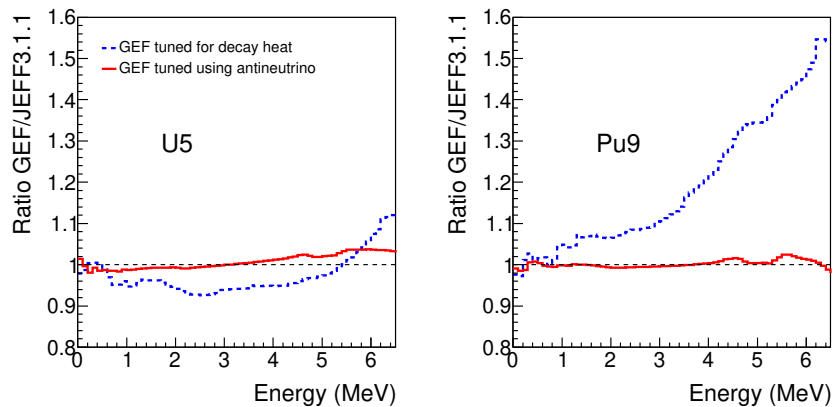


Figure 2: Ratio of the anti-neutrino spectra GEF/JEFF before the tuning (blue line) thanks to antineutrino energy spectra and additional fission yield data and after (red line).

Figure 2 shows the level of agreement that was reached between the anti-neutrino spectra obtained with the GEF predictions and those obtained with the JEFF3.1.1 fission yields with a previous version of GEF that was in good agreement with the integral data of the decay heat after fission pulses of various fissioning systems. The anti-neutrino energy spectra of  $^{235}\text{U}$  and  $^{239}\text{Pu}$  computed with the two sets of fission yields were in agreement only at the 10-30% level even in a restricted energy range up to 6 MeV. The adjustment of the GEF model documented in [25] was performed with a general fit to all mass yields from ENDF/B-VII. This way, data with very different quality, including faulty data, which spoiled the quality of the result, were included in the fit on the same footing. This explains, why the previous version of GEF gave so strongly different anti-neutrino spectra.

The extraction of the list of nuclei contributing importantly to the anti-neutrino energy spectra has allowed to evidence the causes of the remaining discrepancies between GEF and experimental fission yields for these nuclei. The anti-neutrino spectra are particularly sensitive to the yields of specific nuclides, especially at the higher energies. In addition, the relatively large uncertainties of JEFF 3.1.1 and JEFF 3.3 fission yields suggested a good reproduction by the

GEF model with rather large deviations. Deviations inside the error bars of the evaluations lead to substantial variations in the anti-neutrino spectrum. These remaining discrepancies had only little impact on other observables such as the decay heat after fission pulses but revealed to impact a lot the anti-neutrino spectra. Additional experimental constraints were needed, and this conclusion triggered the use of the LOHENGRIN data which eventually allowed to improve a lot the predictiveness of the model because they are much more accurate, as we will show in the section 5 and 6 of this article. The reactor anti-neutrino observable is thus a stringent additional constraint for the evaluation of nuclear data and its combination with the GEF model allows to tackle the source of remaining inconsistencies in the data. It is important to underline here that the GEF parameters have been tuned globally so that these results constrain also all the other predictions for different fissioning systems.

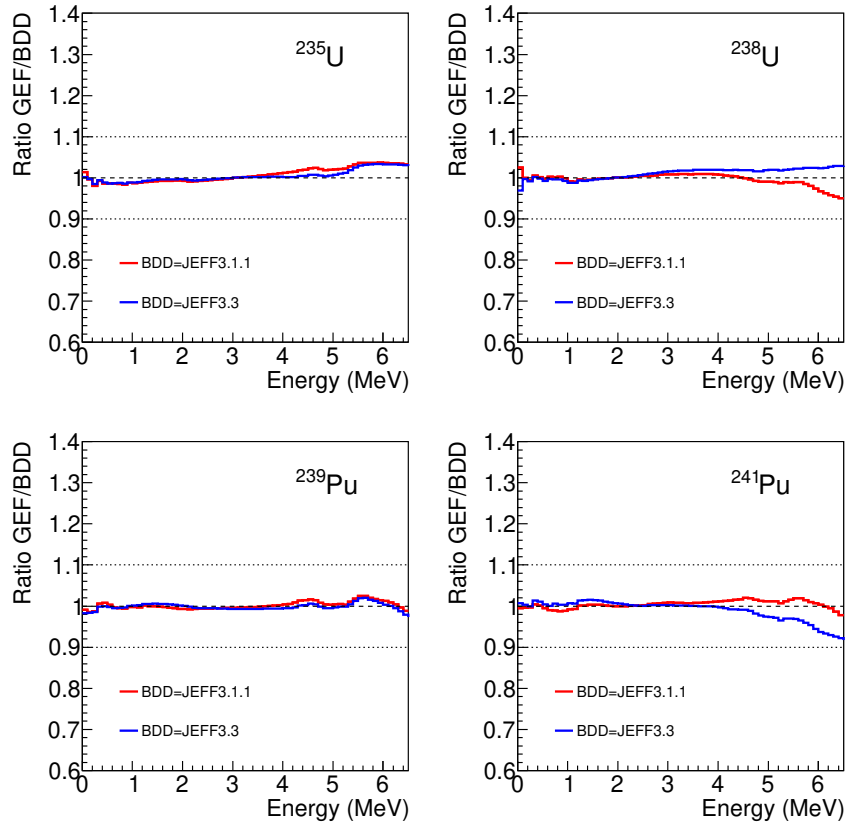


Figure 3: Ratio of the anti-neutrino spectra GEF/JEFF after tuning.

The figure 3 shows the relative ratio of the anti-neutrino energy spectra of  $^{235}\text{U}$ ,  $^{239}\text{Pu}$ ,  $^{241}\text{Pu}$  and  $^{238}\text{U}$  obtained with the cumulative yields computed with

the GEF code in its latest version to those obtained either with the cumulative fission yields of JEFF3.1.1 (red line) or JEFF3.3 (blue line). An agreement at the 2% level is observed with JEFF3.1.1 up to 4 MeV in the four cases. The agreement is also good with JEFF3.3 though it deviates by 3% above 3 MeV in the case of  $^{238}\text{U}$ . Above 4 MeV larger deviations can be observed reaching 4% above 5.5 MeV in the  $^{235}\text{U}$  ratio and 3% in the  $^{239}\text{Pu}$ . In the cases of  $^{241}\text{Pu}$  and  $^{238}\text{U}$ , the discrepancies between the two sets of JEFF fission yields are sensible above 3 MeV, with the largest deviation reached in the case of the JEFF3.3 yields of the  $^{241}\text{Pu}$ .

Overall the level of agreement now reached between the spectra obtained with the GEF predictions and that obtained with the evaluated fission yields has been greatly improved by the adjustment of GEF to empirical data performing a survey on the FYs of all the systems. It is a rather difficult task. Indeed performing a least-square fit to all data does not lead to a satisfactory result, because many evaluated values are erroneous. In some cases, this is evident, but in the majority of cases a careful analysis and a systematic comparison between data from different sources and evaluations and with GEF is needed to sort out the more reliable and the less trustworthy values. We will present in section 4 the experimental methods that led to the available sets of data used to constrain the GEF model, with their advantages and drawbacks. We will then show illustrative examples.

### 3.3 Beta-decay emitters

Using the summation method, the nuclei contributing mainly to the anti-neutrino energy spectra of  $^{235}\text{U}$ ,  $^{239}\text{Pu}$ ,  $^{241}\text{Pu}$  and  $^{238}\text{U}$  have been extracted in bins of anti-neutrino energies. These lists were used to constitute the table 3 extracted from [50], obtained with the JEFF3.1.1 fission yields in the summation model of [19]. In a second table, we have also indicated the fission channel producing dominantly the corresponding nuclei. This piece of information can be deduced from the GEF model and is indicated in the column following each nuclide in table 4.

The table 4 shows that the dominant contributions to the reactor anti-neutrino spectra arise mainly from fission products from the S1 and S2 fission channels. It also shows that the low mass yields are especially important for the computation of the anti-neutrino spectra.

The table 5 shows the relative discrepancies between the GEF, JEFF 3.1.1 and JEFF 3.3 cumulative yields for the top twenty of the largest contributions to the  $^{235}\text{U}$  anti-neutrino energy spectrum. The agreement reached after the complex tuning of the GEF model on the available datasets for a wide set of fissioning systems is quite satisfactory, and mainly constrained by the small uncertainties of the LOHENGRIN data. As will be shown in the next section, the LOHENGRIN fission yields are in good agreement with the JEFF evaluated fission yields in the case of  $^{235}\text{U}$ , but their uncertainties are smaller, which lets us think that the uncertainties of the JEFF yields could be reduced.

Table 3: List of nuclides identified by the IAEA TAGS Consultants that should be measured using the total absorption technique to improve the predictions of the reactor anti-neutrino spectra. These nuclides are of relevance for conventional reactors based on  $^{235}\text{U}$  and  $^{239}\text{Pu}$  nuclear fuels. The list contains 34 nuclides. [50]. Rel. (relevance) stands for the priority of the measurement. Isotopes marked with asterisks show the performed measurements by the Valencia-Nantes collaboration. m stands for metastable or isomeric state.

Isotope	Rel.	Isotope	Rel.	Isotope	Rel.
36-Kr-91	2	39-Y-97m	1	53-I-138*	2
37-Rb-88	1	39-Y-98m	1	54-Xe-139	1
37-Rb-90	1	39-Y-99*	1	54-Xe-141	2
37-Rb-92 *	1	40-Zr-101	1	55-Cs-139	1
37-Rb-93 *	1	41-Nb-98*	1	55-Cs-140*	1
37-Rb-94 *	2	41-Nb-100*	1	55-Cs-141	2
38-Sr-95 *	1	41-Nb-101*	1	55-Cs-142*	1
38-Sr-96	1	41-Nb-102*	1	57-La-146	2
38-Sr-97	2	41-Nb-104m	2		
39-Y-94	1	52-Te-135	1		
39-Y-95*	1	53-I-136	2		
39-Y-96*	1	53-I-136m	1		
39-Y-97	2	53-I-137*	1		

Table 4: List of nuclides contributing importantly to the the reactor anti-neutrino spectra computed with the GEF fission yields. These nuclides are of relevance for conventional reactors based on  $^{235}\text{U}$  and  $^{239}\text{Pu}$  nuclear fuels. In the column next to each nuclide is indicated the fission channel which dominates its production. m stands for metastable or isomeric state.

Isotope	Channel	Isotope	Channel	Isotope	Channel
36-Kr-91	S2	39-Y-97m	S2	53-I-138	S2
37-Rb-88	S2	39-Y-98m	S2	54-Xe-139	S2
37-Rb-90	S2	39-Y-99	S2 and S1	54-Xe-141	S2
37-Rb-92	S2	40-Zr-101	S2 and S1	55-Cs-139	S2
37-Rb-93	S2	41-Nb-98	S2	55-Cs-140	S2
37-Rb-94	S2	41-Nb-100	S2 and S2	55-Cs-141	S2
38-Sr-95	S2	41-Nb-101	S2 and S1	55-Cs-142	S2
38-Sr-96	S2	41-Nb-102	S2 and S1	57-La-146	S2
38-Sr-97	S2	41-Nb-104m	S2 and S1		
39-Y-94	S2	52-Te-135	S2 and S1		
39-Y-95	S2	53-I-136	S2 and S1		
39-Y-96	S2	53-I-136m	S2 and S1		
39-Y-97	S2	53-I-137	S2		

Table 5: List of the 20 nuclides contributing most importantly to the the  $^{235}\text{U}$  anti-neutrino spectrum in the 4 to 5 MeV bin ordered by importance of contribution obtained with the fission yields of JEFF3.1.1. In the two next columns are indicated the absolute relative discrepancy of the GEF fission yields to the JEFF3.1.1 and JEFF3.3 evaluated cumulative yields.

Isotope	Rel. Dif. GEF vs JEFF3.1.1	Rel. Dif. GEF vs JEFF3.3
39-Y-95	5.4%	6.5%
39-Y-94	9.4%	9.5%
38-Sr-93	0.6%	0.4%
55-Cs-139	2.8%	3.9%
55-Cs-140	2.8%	0.23%
57-La-142	2.1%	2.4%
41-Nb-98	5.7%	5.8%
37-Rb-91	9.4%	5.7%
41-Nb-100	1.2%	2.8%
57-La-144	9.0%	9.0%
38-Sr-95	7.6%	6.7%
54-Xe-139	3.6%	5.1%
41-Nb-101	0.2%	3.3%
36-Kr-90	12.3%	8.9%
55-Cs-141	2.0%	3.1%
37-Rb-92	0.02%	10.5%
39-Y-96	25.9	27.5%%
37-Rb-89	4.2%	4.8%
36-Kr-89	3.9%	4.0%
37-Rb-90	6.0%	2.6%

In addition to calculating the so-far presented yields of the secondary fragments resulting from the de-excitation of the primary fragments produced at scission, the GEF model can compute their radioactive decay whenever it applies. Hence, the code can provide a complete overview on the contributions of the various fragments to the beta spectrum, sorted by the Q value. The four figures 4 show the calculated intensities and the Q values of the beta decays of the different fragments on their radioactive decay towards beta stability on the chart of the nuclides for the four systems  $^{235}\text{U}(n_{th},f)$ ,  $^{238}\text{U}(n_{fast},f)$ ,  $^{239}\text{Pu}(n_{th},f)$  and  $^{241}\text{Pu}(n_{th},f)$ .

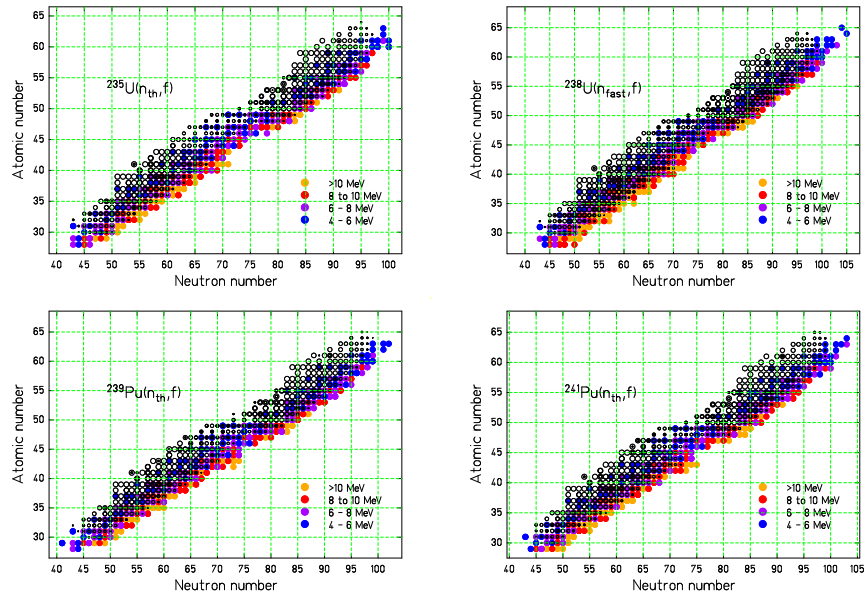


Figure 4: Contributions of the individual fragments to the beta decays for the systems  $^{235}\text{U}(n_{th},f)$ ,  $^{238}\text{U}(n_{fast},f)$ ,  $^{239}\text{Pu}(n_{th},f)$  and  $^{241}\text{Pu}(n_{th},f)$  calculated with the GEF code. The size of the black circles corresponds to the magnitude over four orders of magnitude in a logarithmic scale, and the color indicates the Q-value range.

Expecting that the average decay energies are strongly correlated with the  $Q$  value, the highest decay energies are, on the average, found in the light fragment group with an odd-even staggering that enhances the decay energies of the odd elements. The high decay energies and presumably also the high-energy part of the anti-neutrino spectrum are dominated by contributions of the odd- $Z$  elements from  $Z = 31$  to  $Z = 37$ .

As expected, one observes a shift to more exotic nuclides with a tendency to longer beta-decay chains with increasing neutron excess of the fissioning system. This goes in line with an enhancement of higher decay energies.  $^{238}\text{U}(n_{fast},f)$  provides the highest contributions to the high-energy part of the spectrum, because it is the most neutron-rich system. A detailed comparison of this information with the information on the accuracy of the fission-fragment yields, discussed in the preceding sections, provides a good basis for revealing the contributions of individual fission-yield uncertainties to the uncertainties of calculated anti-neutrino spectra.

## 4 Experimental approaches

The fission process ends up in two fission fragments, which populate about thousand different nuclides. (We do not consider ternary fission here, where a third light particle is formed in addition with low probability.) Several experimental approaches have been developed for measuring the yields of the different fragments formed in the fission of a specific nucleus at a certain excitation energy and angular momentum. We will consider some of those, which are most often used. See ref. [51] for an extensive overview on presently used experimental approaches in fission.

### 4.1 Radio-chemistry

#### 4.1.1 The method

The traditional method for measuring fission-fragment yields consists of exposing samples to a flux of neutrons. After irradiation, the samples are investigated by gamma spectroscopy [52]. The fission fragments are identified unambiguously in  $Z$  and  $A$  by measuring the gammas emitted directly or in their radioactive decay chain, and their yields are deduced from the intensities of the gamma lines. Chemical separation is often applied in order to purify the gamma spectra by reducing the background radiation.

#### 4.1.2 Independent and cumulative yields

The primary fission fragments, as they are formed at scission, normally carry some excitation energy that gives rise to a cascade of prompt neutrons and prompt gammas, until the ground state or a longer-lived isomeric state is reached. (Processes are called to be prompt, if they occur inside a certain time window

that is much shorter than typical beta-decay half-lives, which are in the millisecond range. The exact definition can differ.) The fission-fragment yields after the prompt processes are called independent yields.

Only the gamma radiation emitted in a time range of a few seconds (or longer) after fission, which is needed for the extraction of the target and, eventually, the chemical separation, can be measured by radiochemistry. Therefore, the yields of the especially short-lived most neutron-rich fragments cannot be determined directly.

The yields of the products of the consecutive radioactive decay are called cumulative yields. Because beta-delayed neutron emission that changes the nuclear mass number is a rare process, the last cumulative yields at the beta stability are a good measure of the mass yields. Thus, the mass yields can be measured with rather high accuracy.

### 4.1.3 Yields of short-lived fragments

Methods have been developed to determine even the independent yields of short-lived radioactive fragments by requiring consistency between the neutron-deficient wing of the nuclide distribution in the light fragment and the neutron-rich wing of the nuclide distribution in the heavy fragment (and vice versa) with the mass-dependent multiplicity of prompt neutrons [53]. The application of this method on the basis of incomplete or even fragmentary experimental data requires a good knowledge of the behaviour of fission-fragment nuclide distributions and prompt-neutron multiplicities. One of the most popular systematics used for this purpose has been developed by Wahl [54].

### 4.1.4 Strengths and weaknesses

The main strength of the radio-chemical method is the unambiguous identification of the fission fragments in  $Z$  and  $A$ . Also the sensitivity down to very low yields is a strength of this method.

However, there are several weaknesses of this method: Due to the time delay between irradiation and measurement, this method is slower than the life times of many fission fragments, in particular of the most neutron-rich ones. Therefore, the independent yields of short-lived fragments cannot directly be measured, and their indirect determination (see above) depends on certain assumptions.

Another weakness is the uncertainty introduced by the uncertainty of the spectroscopic information that is used to infer the number of fission fragments from the intensities of the gamma lines. Also mis-identification of a gamma line can lead to erroneous results. Moreover, target impurities may be an issue.

The application of this method is limited to suitable targets and available neutron sources with suitable energies. Most available data were obtained with thermal neutrons, fission neutrons with energies around 1 MeV that they obtain in the evaporation process, eventually partly moderated, and with 14-MeV neutrons.

## 4.2 Experiments with particle detectors in direct kinematics

### 4.2.1 The method

Instead of exploiting the radioactivity of the fission fragments with the radiochemical method, their high kinetic energies have been used to detect and identify the fission fragments by their ionization signals in different kind of detectors. This way, the energy loss in thin detectors, the total energy in thick detectors, or the time-of-flight between two detectors were measured, eventually those of both fission fragments simultaneously. However, only by the additional measurement of the deflection in the electric and/or magnetic field in powerful spectrometers, the resolution in  $Z$  and  $A$  was sufficient to determine the yields of individual nuclides. We consider here the LOHENGRIN spectrometer [55], where the full mass distribution and the  $Z$  distribution in the lighter fragment were measured for the thermal-neutron-induced fission of a few systems.

### 4.2.2 Strengths and weaknesses

A great advantage of kinematical measurements at the LOHENGRIN spectrometer is the rather direct determination of fission-fragment yields by ion counting. There is no need to account for detection efficiencies. Nevertheless, a few corrections must be applied in order to account for the burn-up of the target material and the deterioration of the target quality by diffusion of the target material into the backing [56]. Furthermore, the fragments appear with a distribution of ionic charge states. These distributions have to be measured separately, and the associated yields have to be added up. A peculiar difficulty consists in the shift of the ionic charge-state distribution due to internal conversion and a consecutive Auger cascade for specific nuclides [57]. These cannot be calculated with sufficient accuracy and must be determined experimentally by a scan over the charge-state distribution of all fission fragments. Therefore, a good quality of the data requires a very careful analysis and correction of these disturbing effects.

In addition to the limitation to thermal-neutron-induced fission of a few suitable target nuclei, the kinetic-energy distribution of the fragments cannot be covered completely by practical reasons. The full distribution must be estimated from the measurements at a few kinetic-energy values. This may introduce some systematic uncertainties.

## 4.3 Experiments with particle detectors in inverse kinematics

### 4.3.1 The method

During the last years, an innovative experimental approach has been introduced [58, 59, 60]: The fissioning nucleus is prepared with high kinetic energies, and,

thus, the fragments are emitted with velocities that are appreciably higher than those, which they get in the fission process in direct kinematics.

### 4.3.2 Strengths and weaknesses

Excellent resolution in  $A$  and  $Z$  has been obtained, but, partly due to the insufficiently well defined initial excitation energy of the fissioning system, the results have not yet been exploited so much for extracting nuclear data for technical applications. Therefore, we mention this method only for completeness and for its growing importance in the future, but we will not consider this method here further.

## 5 Evaluations

Evaluation assesses the measured data and their uncertainties, reconciles discrepant experimental data and fills in missing data by exploiting systematic trends of the measured data in order to provide reliable nuclear data, primarily for applications in nuclear technology. Evaluation work is organized, and the resulting nuclear-data tables are disseminated by several nuclear data centers under the auspices of the International Atomic Energy Agency.

In the following, we will consider the evaluations ENDF/B-VII, JEFF 3.1.1 and JEFF 3.3. The main sources of these evaluations are data from radiochemical measurements, supplemented by only a few data from LOHENGRIN experiments, in spite of their special advantages in accuracy. Theoretical fission models have been exploited only very little up to now.

## 6 Comparative study

In this study, we compare the fission-fragment mass distributions for thermal-neutron-induced fission of all systems, which are included in the ENDF/B-VII, the JEFF 3.1.1 or the JEFF 3.3 evaluation or for which experimental data from LOHENGRIN experiments are available, with the result of the GEF code. In addition, a few mass distributions for fast-neutron-induced fission are included. For a quick overview of the essential results, important conclusions and recommendations are given in *italic*.

### 6.1 Overall impression

In the present section 6.1, the mass yields from the GEF code are compared with evaluated data or results from LOHENGRIN experiments, where at least satisfactory agreement has been obtained. At the same time, these are the systems that have been experimentally investigated the most intensively, and the data are expected to be the most reliable. Cases with larger deviations

are discussed in section 6.2. We concentrate here mostly on thermal-neutron-induced and fast-neutron-induced fission. A more general overview is given in ref. [25], however with a less elaborate version of the GEF code.

Systematic comparisons of the independent yields from the GEF code with the JEFF 3.3 evaluation for a number of selected systems are shown and discussed in the appendix.

Eventually we came up with the following rules:

1. Radiochemical data have very different quality. By far the most reliable ones are the FY for  $^{235}\text{U}(\text{n}_{th},\text{f})$ , followed by  $^{239}\text{Pu}(\text{n}_{th},\text{f})$  and very few other systems. The data of all other systems are less trustworthy. The quality is not always reflected by the error bars.
2. Mass yields from LOHENGRIN experiments are much more accurate than those from radiochemical measurements (with one exception).
3. Indirect information on FY (anti-neutrino spectrum, decay heat etc.) are extremely sensitive probes for the over-all quality of the FYs for specific systems.
4. It is important to primarily adjust the parameters of GEF to the most trustworthy data. The regularities of GEF help to recognize faulty data of other systems.

These rules were applied very strictly for the first time in this work.

### 6.1.1 Illustrative cases

**Mass yields in  $^{229}\text{Th}(\text{n}_{th},\text{f})$ :** Figures 5, 6, 7, and 8 show comparisons of the mass yields from GEF with the data from the ENDF/B-VII evaluation and from a LOHENGRIN experiment [61] for the system  $^{229}\text{Th}(\text{n}_{th},\text{f})$ . There is fair agreement, except some underestimated intensities of the peaks near  $A = 85$  and  $A = 144$ . These deviations hint to a *problem in the description of the S2 fission channel in GEF*. This problem might be cured by the introduction of a more complex shape of the S2 contribution to the mass yields. However, this is beyond the scope of the present status of GEF, because a higher degree of complexity and the corresponding introduction of additional model parameters might endanger the predictive power of the model. The symmetric yield is slightly overestimated.

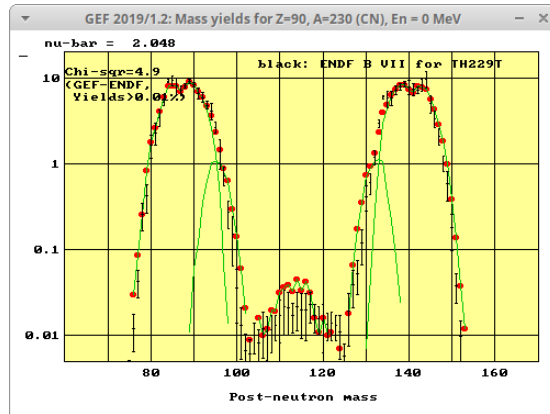


Figure 5: Mass yields of  $^{229}\text{Th}(n_{th},f)$ , logarithmic scale, GEF result (red points) in comparison with ENDF/B-VII (black symbols with error bars). Here and in the following figures, the green lines show the contributions of the different fission channels from GEF.

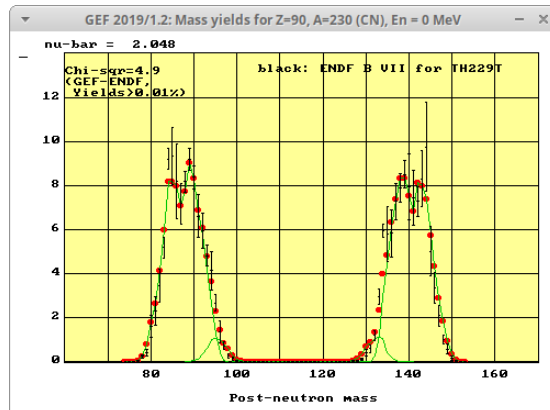


Figure 6: Mass yields of  $^{229}\text{Th}(n_{th},f)$ , linear scale, GEF result (red points) in comparison with ENDF/B-VII (black symbols).

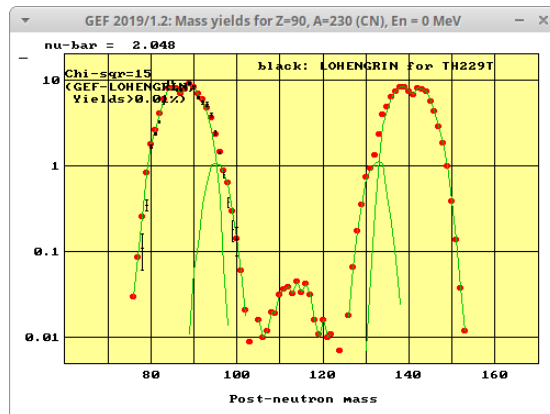


Figure 7: Mass yields of  $^{229}\text{Th}(n_{th},f)$ , logarithmic scale, GEF result (red points) in comparison with the data of a LOHENGRIN experiment (black symbols).

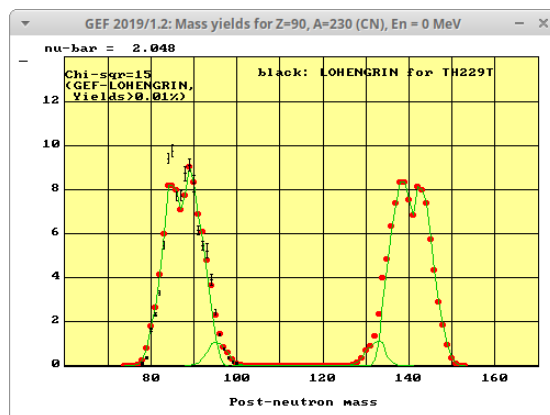


Figure 8: Mass yields of  $^{229}\text{Th}(n_{th},f)$ , linear scale, GEF result (red points) in comparison with the data of a LOHENGRIN experiment (black symbols).

**Mass yields in  $^{233}\text{U}(\text{n}_{th},\text{f})$ :** Figures 9, 10, 11, 12, 13, 14, 15, and 16 show comparisons of the mass yields from GEF with the data from the ENDF/B-VII, JEFF 3.1.1 and JEFF 3.3 evaluations, as well as from a LOHENGRIN experiment [62] for the system  $^{233}\text{U}(\text{n}_{th},\text{f})$ . There is fair agreement. However, the yields near  $A = 90$  and  $A = 136$  are somewhat underestimated, while the yields near  $A = 98$  are somewhat overestimated. In addition, the yields in the inner wing of the asymmetric peaks are somewhat underestimated. *These discrepancies* appear with respect to the data from all sources. Thus, they *must probably be attributed to deficiencies of GEF*, probably due to restrictions in the shape of the asymmetric fission channels. This is in line with the observations for the system  $^{229}\text{Th}(\text{n}_{th},\text{f})$ . In spite of differences between the evaluations, the yield at symmetry seems to be slightly overestimated. In addition, its shape is concave, while evaluations suggest a more flat, or even convex, pattern.

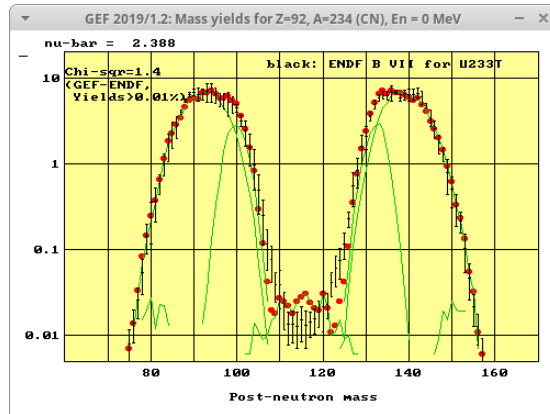


Figure 9: Mass yields of  $^{233}\text{U}(n_{th},f)$ , logarithmic scale, GEF result (red points) in comparison with ENDF/B-VII (black symbols).

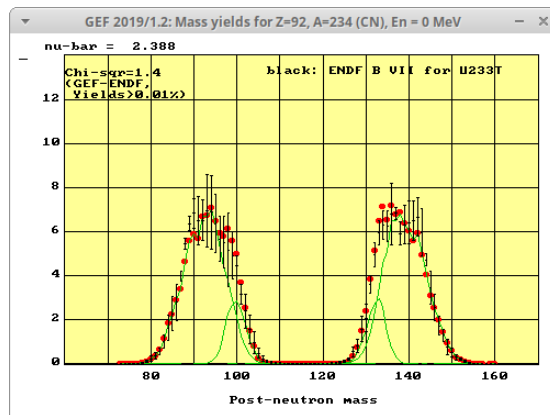


Figure 10: Mass yields of  $^{233}\text{U}(n_{th},f)$ , linear scale, GEF result (red points) in comparison with ENDF/B-VII (black symbols).

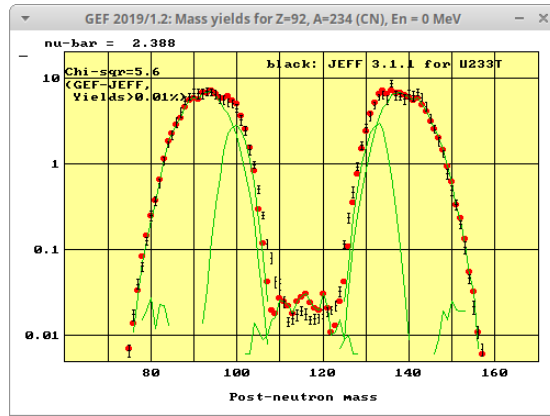


Figure 11: Mass yields of  $^{233}\text{U}(n_{th},f)$ , logarithmic scale, GEF result (red points) in comparison with JEFF 3.1.1 (black symbols).

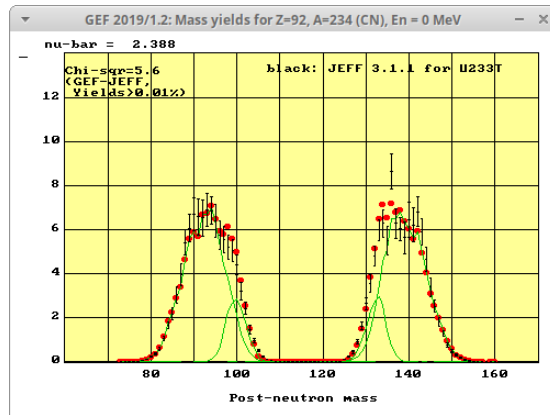


Figure 12: Mass yields of  $^{233}\text{U}(n_{th},f)$ , linear scale, GEF result (red points) in comparison with JEFF 3.1.1 (black symbols).

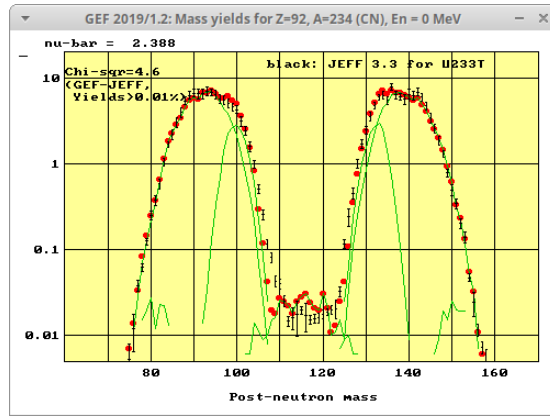


Figure 13: Mass yields of  $^{233}\text{U}(n_{th},f)$ , logarithmic scale, GEF result (red points) in comparison with JEFF 3.3 (black symbols).

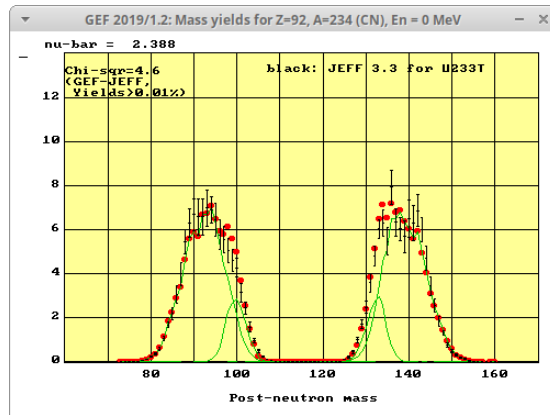


Figure 14: Mass yields of  $^{233}\text{U}(n_{th},f)$ , linear scale, GEF result (red points) in comparison with JEFF 3.3 (black symbols).

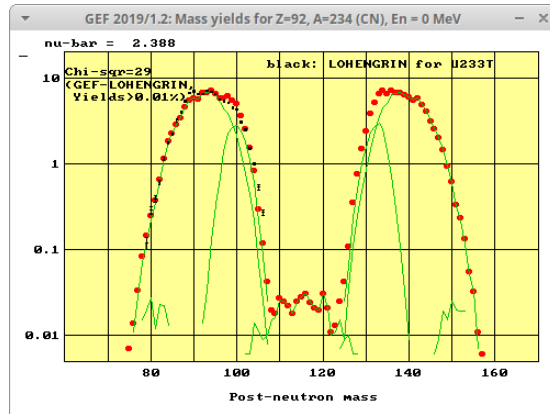


Figure 15: Mass yields of  $^{233}\text{U}(n_{th},f)$ , logarithmic scale, GEF result (red points) in comparison with data from a LOHENGRIN experiment (black symbols).

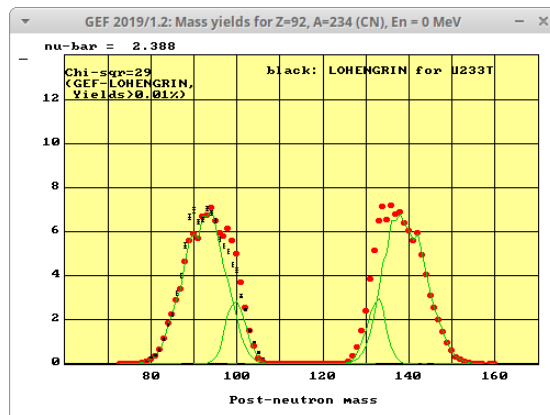


Figure 16: Mass yields of  $^{233}\text{U}(n_{th},f)$ , linear scale, GEF result (red points) in comparison with data from a LOHENGRIN experiment (black symbols).

**Mass yields in  $^{235}\text{U}(\mathbf{n}_{th}, \mathbf{f})$ :** Figures 17, 18, 19, 20, 21, 22, 23, and 24 show comparisons of the mass yields from GEF with the data from the ENDF/B-VII, JEFF 3.1.1 and JEFF 3.3 evaluations, as well as from LOHENGRIN experiments [63, 64] for the system  $^{235}\text{U}(\mathbf{n}_{th}, \mathbf{f})$ , which is the most intensively studied and best known system of all.

The data of all evaluations are rather well reproduced. The smallest deviations are found with respect to the LOHENGRIN data, which have by far the smallest uncertainties. The deviations appear in slightly underestimated yields around  $A = 90$  and slightly overestimated yields around  $A = 94$ , which again hints to some *shortcoming in the shape of the  $S2$  fission channel in GEF*. Moreover some yields in the extremely asymmetric splits are overestimated, where the super-asymmetric fission mode dominates. We note that the yield at symmetry is very slightly overestimated, but better reproduced than for  $^{233}\text{U}(\mathbf{n}_{th}, \mathbf{f})$ .

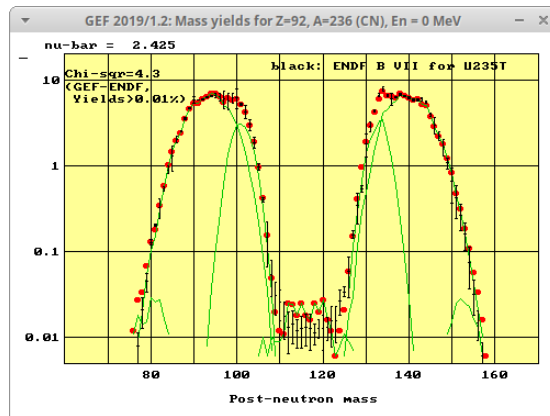


Figure 17: Mass yields of  $^{235}\text{U}(n_{th},f)$ , logarithmic scale, GEF result (red points) in comparison with ENDF/B-VII (black symbols).

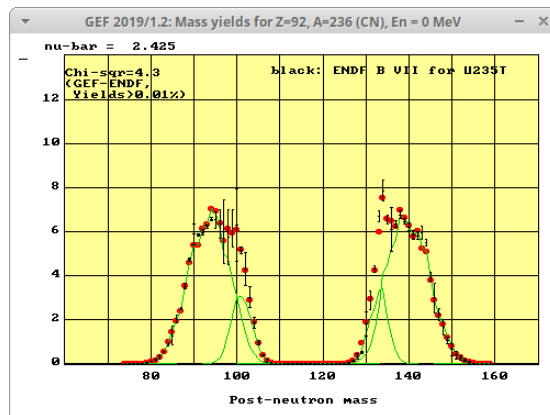


Figure 18: Mass yields of  $^{235}\text{U}(n_{th},f)$ , linear scale, GEF result (red points) in comparison with ENDF/B-VII (black symbols).

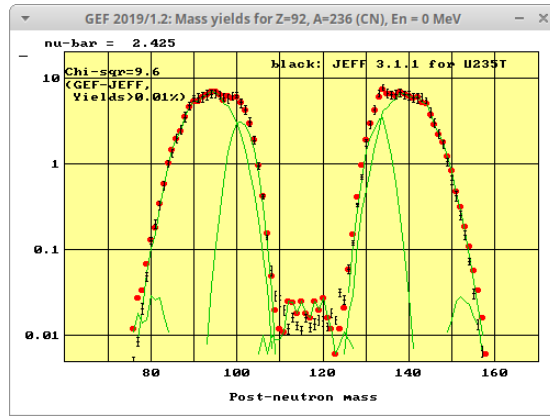


Figure 19: Mass yields of  $^{235}\text{U}(n_{th},f)$ , logarithmic scale, GEF result (red points) in comparison with JEFF 3.1.1 (black symbols).

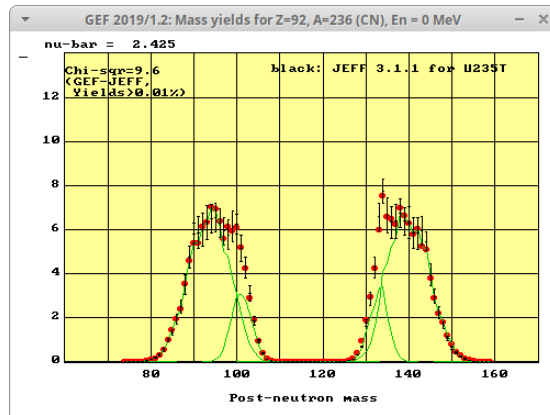


Figure 20: Mass yields of  $^{235}\text{U}(n_{th},f)$ , linear scale, GEF result (red points) in comparison with JEFF 3.1.1 (black symbols).

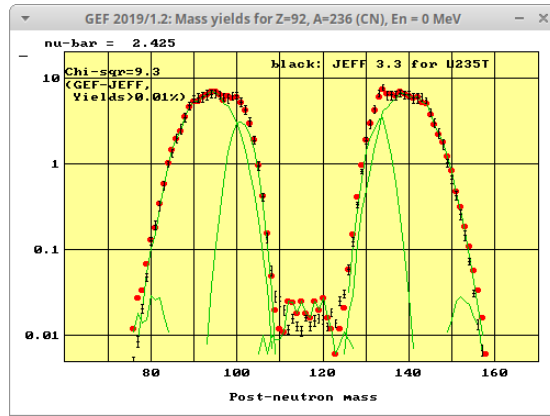


Figure 21: Mass yields of  $^{235}\text{U}(n_{th},f)$ , logarithmic scale, GEF result (red points) in comparison with JEFF 3.3 (black symbols).

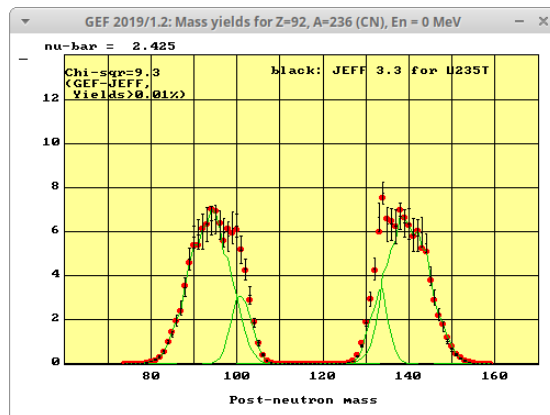


Figure 22: Mass yields of  $^{235}\text{U}(n_{th},f)$ , linear scale, GEF result (red points) in comparison with JEFF 3.3 (black symbols).

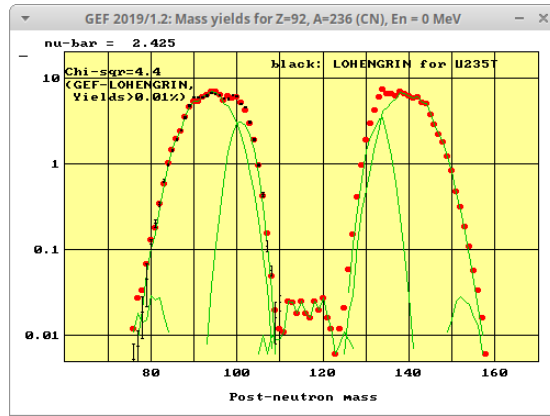


Figure 23: Mass yields of  $^{235}\text{U}(n_{th},f)$ , logarithmic scale, GEF result (red points) in comparison with data from a LOHENGRIN experiment (black symbols).

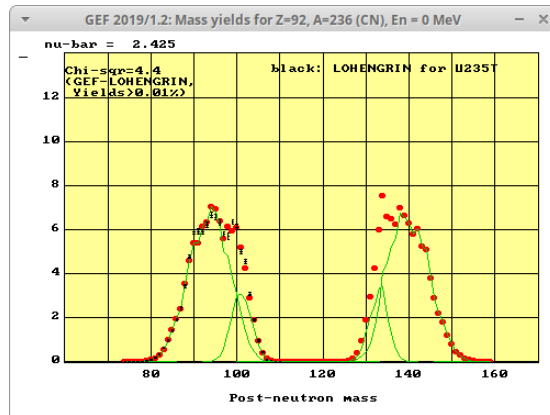


Figure 24: Mass yields of  $^{235}\text{U}(n_{th},f)$ , linear scale, GEF result (red points) in comparison with data from a LOHENGRIN experiment (black symbols).

**Mass yields in  $^{238}\text{Np}(n_{th},f)$ :** Figures 25, 26, 27, 28, 29, and 30 show comparisons of the mass yields from GEF with the data from the ENDF/B-VII, JEFF 3.1.1 and JEFF 3.3 evaluations, as well as from LOHENGRIN experiments [65, 66] for the system  $^{238}\text{Np}(n_{th},f)$ . Again, the LOHENGRIN data have the smallest uncertainties. The data are quite well reproduced. Some deviations are found in the inner wings of the asymmetric peaks. The yield at symmetry is overestimated.

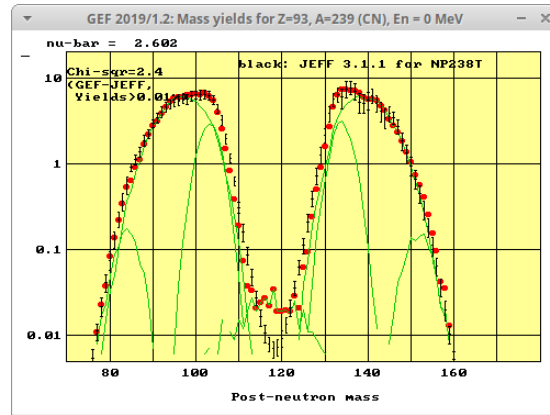


Figure 25: Mass yields of  $^{238}\text{Np}(n_{th},f)$ , logarithmic scale, GEF result (red points) in comparison with JEFF 3.1.1 (black symbols).

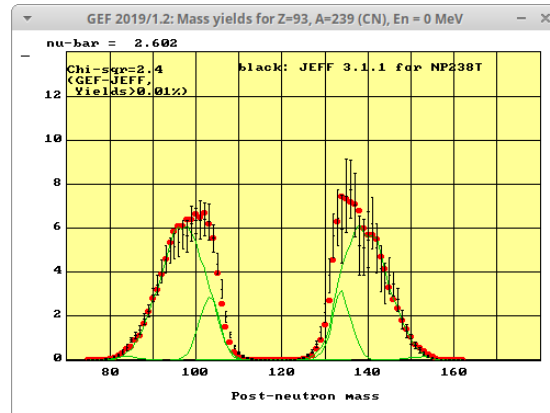


Figure 26: Mass yields of  $^{238}\text{Np}(n_{th},f)$ , linear scale, GEF result (red points) in comparison with JEFF 3.1.1 (black symbols).

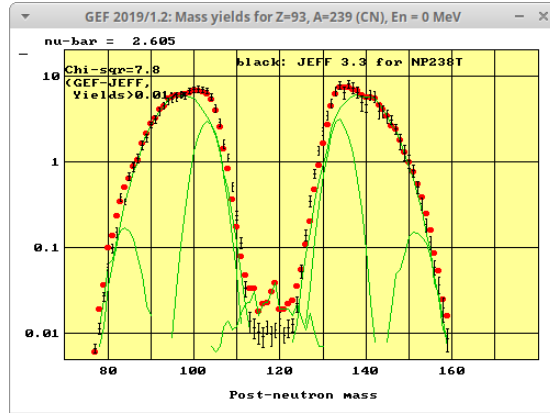


Figure 27: Mass yields of  $^{238}\text{Np}(n_{th},f)$ , logarithmic scale, GEF result (red points) in comparison with JEFF 3.3 (black symbols).

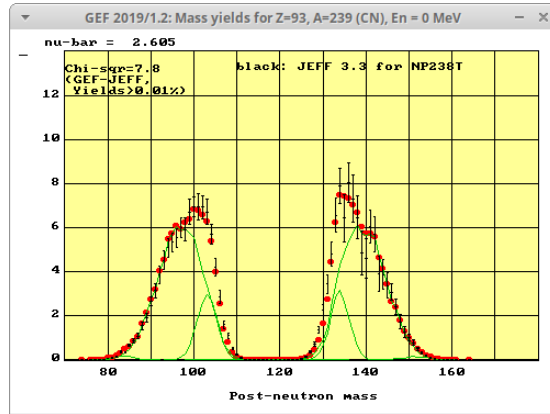


Figure 28: Mass yields of  $^{238}\text{Np}(n_{th},f)$ , linear scale, GEF result (red points) in comparison with JEFF 3.3 (black symbols).

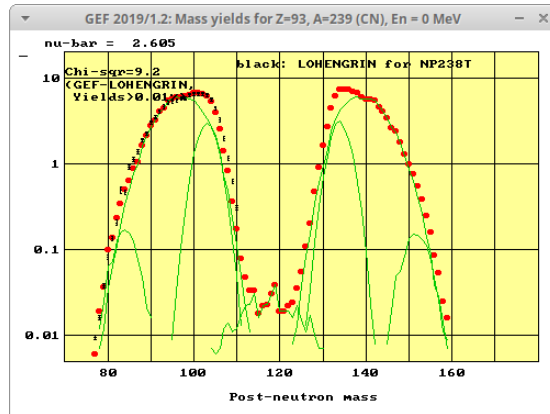


Figure 29: Mass yields of  $^{238}\text{Np}(n_{th},f)$ , logarithmic scale, GEF result (red points) in comparison with data from a LOHENGRIN experiment (black symbols).

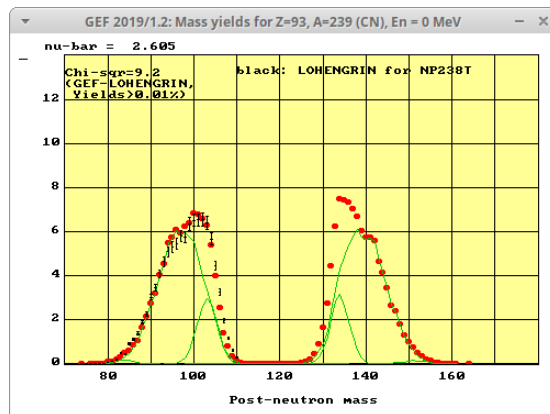


Figure 30: Mass yields of  $^{238}\text{Np}(n_{th},f)$ , linear scale, GEF result (red points) in comparison with data from a LOHENGRIN experiment (black symbols).

**Mass yields in  $^{238}\text{Pu}(n_{th},f)$ :** In figures 31 and 32, the mass yields from GEF are compared with the data from the JEFF 3.3 evaluation for the system  $^{238}\text{Pu}(n_{th},f)$ . There are some deviations between JEFF 3.3 and GEF in the position of the asymmetric peaks: In GEF they are shifted to larger asymmetries. These deviations are astonishing, because the mass yields of the neighbouring system  $^{239}\text{Pu}(n_{th},f)$  are very well reproduced (see below). *Further investigations are needed* to reveal the origin of this problem. We note the reasonable description (height and shape) of the symmetric yield.

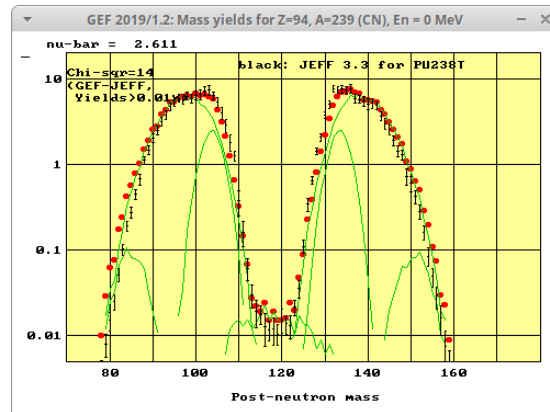


Figure 31: Mass yields of  $^{238}\text{Pu}(n_{th},f)$ , logarithmic scale, GEF result (red points) in comparison with JEFF 3.3 (black symbols).

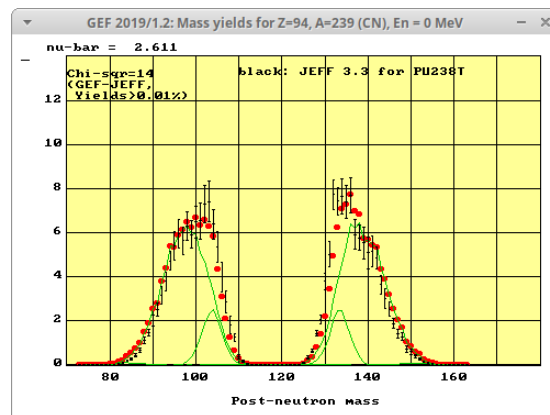


Figure 32: Mass yields of  $^{238}\text{Pu}(n_{th},f)$ , linear scale, GEF result (red points) in comparison with JEFF 3.3 (black symbols).

**Mass yields in  $^{239}\text{Pu}(\mathbf{n}_{th},\mathbf{f})$ :** Figures 33, 34, 35, 36, 37, 38, 39, and 40 show comparisons of the mass yields from GEF with the data from the ENDF/B-VII, JEFF 3.1.1 and JEFF 3.3 evaluations, as well as from a LOHENGRIN experiment [67] for the system  $^{239}\text{Pu}(\mathbf{n}_{th},\mathbf{f})$ . The data of all evaluations are rather well reproduced. The smallest deviations are found with respect to the LOHENGRIN data, which have by far the smallest uncertainties. We would like to draw the attention to an interesting detail: In the LOHENGRIN data there appears a clear shoulder at  $A = 84$ , which is well reproduced by GEF. According to GEF, this shoulder marks the transition from the S2 to the super-asymmetric fission channel. This shoulder does not appear in the evaluations. This shoulder appears, less pronounced, also in the GEF results for  $^{241}\text{Pu}$ , see section 5.2.6. We note the good description around symmetry, namely when compared to ENDF/B-VII.

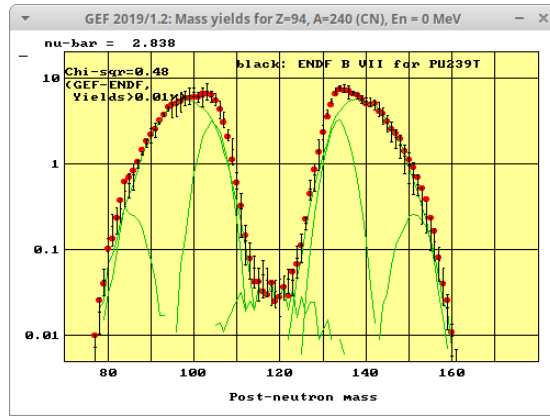


Figure 33: Mass yields of  $^{239}\text{Pu}(n_{th},f)$ , logarithmic scale, GEF result (red points) in comparison with ENDF/B-VII (black symbols).

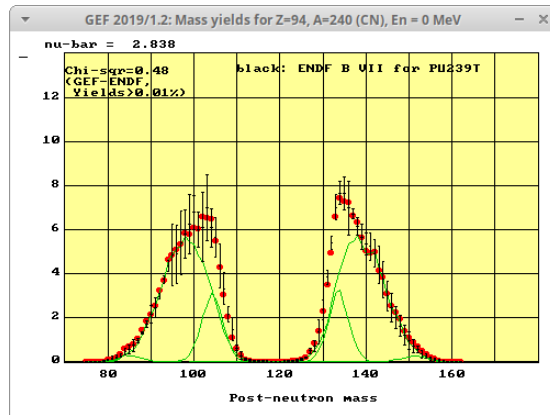


Figure 34: Mass yields of  $^{239}\text{Pu}(n_{th},f)$ , linear scale, GEF result (red points) in comparison with ENDF/B-VII (black symbols).

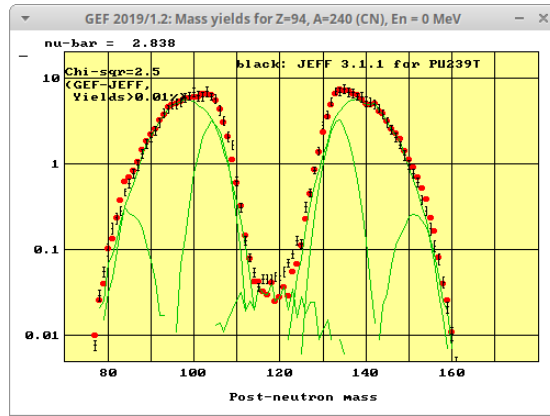


Figure 35: Mass yields of  $^{239}\text{Pu}(n_{th},f)$ , logarithmic scale, GEF result (red points) in comparison with JEFF 3.1.1 (black symbols).

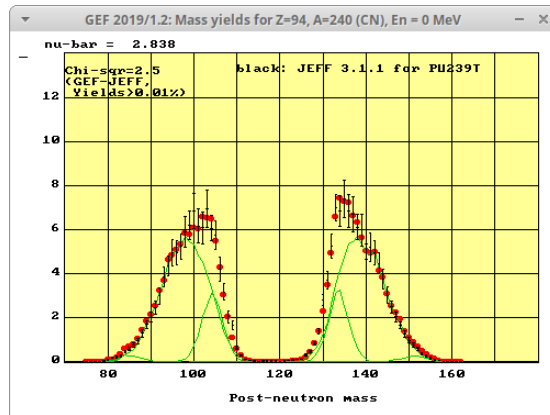


Figure 36: Mass yields of  $^{239}\text{Pu}(n_{th},f)$ , linear scale, GEF result (red points) in comparison with JEFF 3.1.1 (black symbols).

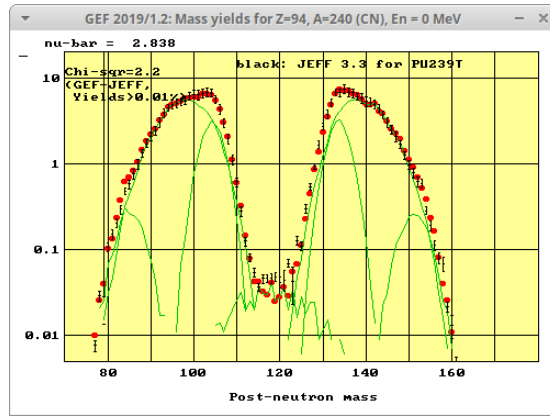


Figure 37: Mass yields of  $^{239}\text{Pu}(n_{th},f)$ , logarithmic scale, GEF result (red points) in comparison with JEFF 3.3 (black symbols).

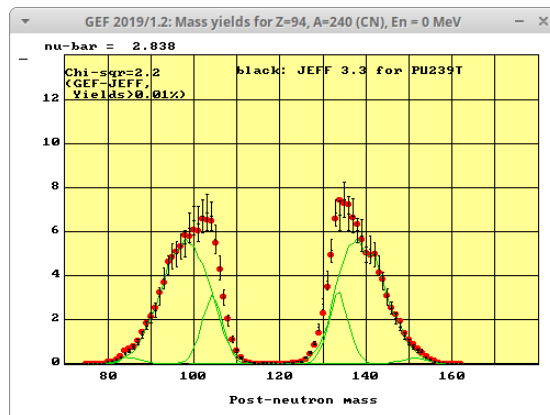


Figure 38: Mass yields of  $^{239}\text{Pu}(n_{th},f)$ , linear scale, GEF result (red points) in comparison with JEFF 3.3 (black symbols).

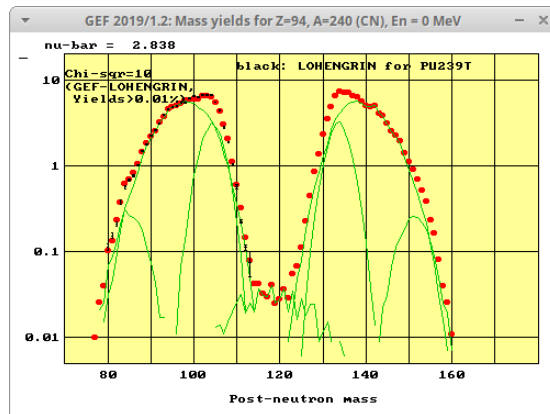


Figure 39: Mass yields of  $^{239}\text{Pu}(n_{th},f)$ , logarithmic scale, GEF result (red points) in comparison with data from a LOHENGRIN experiment (black symbols).

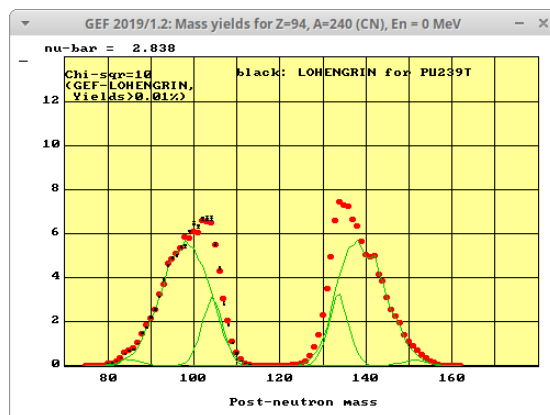


Figure 40: Mass yields of  $^{239}\text{Pu}(n_{th},f)$ , linear scale, GEF result (red points) in comparison with data from a LOHENGRIN experiment (black symbols).

**Mass yields in  $^{240}\text{Pu}(n_{th},f)$ :** Figures 41 and 42 show the comparison of the mass yields from GEF with the data from the ENDF/B-VII for the system  $^{240}\text{Pu}(n_{th},f)$ . The data are rather well reproduced, except near symmetry, where the yields from GEF are lower.

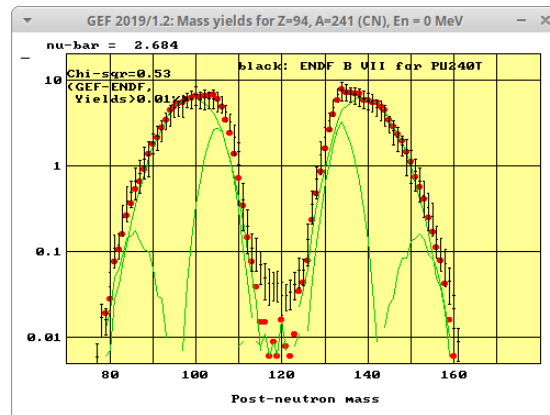


Figure 41: Mass yields of  $^{240}\text{Pu}(n_{th},f)$ , logarithmic scale, GEF result (red points) in comparison with ENDF/B-VII (black symbols).

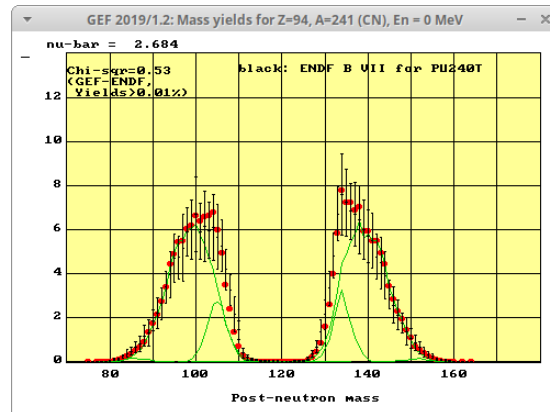


Figure 42: Mass yields of  $^{240}\text{Pu}(n_{th},f)$ , linear scale, GEF result (red points) in comparison with ENDF/B-VII (black symbols).

**Mass yields in  $^{242}\text{Pu}(n_{th},f)$ :** Figures 43 and 44 show the comparison of the mass yields from GEF with the data from the ENDF/B-VII for the system  $^{242}\text{Pu}(n_{th},f)$ . The data are rather well reproduced, except near symmetry, where the yields from GEF are lower.

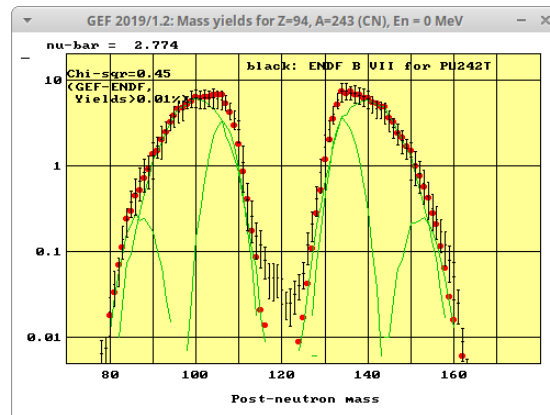


Figure 43: Mass yields of  $^{242}\text{Pu}(n_{th},f)$ , logarithmic scale, GEF result (red points) in comparison with ENDF/B-VII (black symbols).

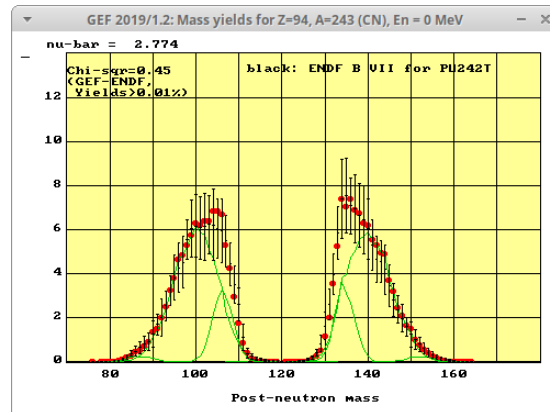


Figure 44: Mass yields of  $^{242}\text{Pu}(n_{th},f)$ , linear scale, GEF result (red points) in comparison with ENDF/B-VII (black symbols).

**Mass yields in  $^{241}\text{Am}(\text{n}_{th},\text{f})$ :** Figures 45, 46, 47, 48, 49, and 50 show the comparison of the mass yields from GEF with the data from ENDF/B-VII, JEFF 3.1.1 and JEFF 3.3 for the system  $^{241}\text{Am}(\text{n}_{th},\text{f})$ . The data are rather well reproduced. Some deviations appear near symmetry and in the upper wing of the distribution. However, *the origin of these deviations is not clear*, because there are also discrepancies between the different evaluations: The symmetric yields from JEFF 3.1.1 and some data in the upper wing from JEFF 3.3 agree with the GEF results. Moreover, the physics connects the yields in the two outer wings with the mass-dependent prompt-neutron yields: A shift in the upper wing to higher masses with respect to GEF, while keeping the lower wing unchanged, as suggested by the evaluations for  $^{241}\text{Am}(\text{n}_{th},\text{f})$  demands a reduction of the prompt-neutron yields in the heavy-mass region with respect to the systematics of other systems, for example  $^{239}\text{Pu}(\text{n}_{th},\text{f})$ , where the mass yields from GEF agree with the empirical data over the whole mass range.

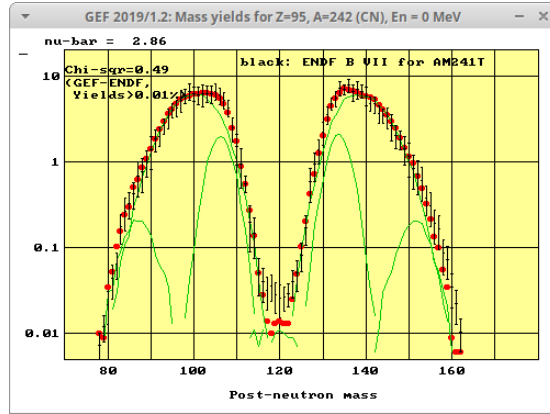


Figure 45: Mass yields of  $^{241}\text{Am}(n_{th},f)$ , logarithmic scale, GEF result (red points) in comparison with ENDF/B-VII (black symbols).

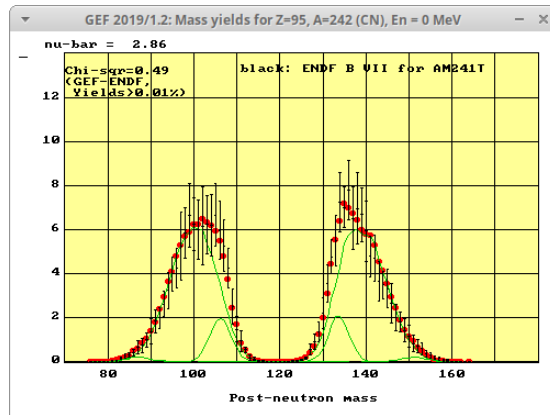


Figure 46: Mass yields of  $^{241}\text{Am}(n_{th},f)$ , linear scale, GEF result (red points) in comparison with ENDF/B-VII (black symbols).

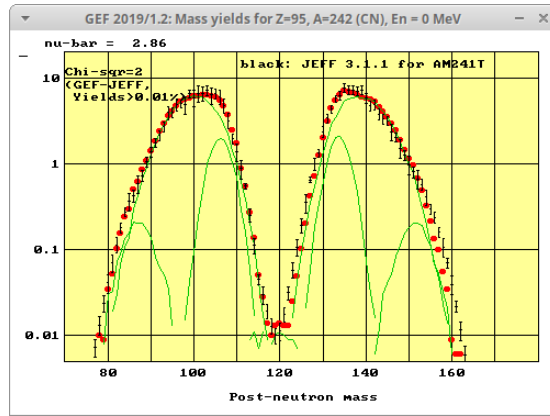


Figure 47: Mass yields of  $^{241}\text{Am}(n_{th},f)$ , logarithmic scale, GEF result (red points) in comparison with JEFF 3.1.1 (black symbols).

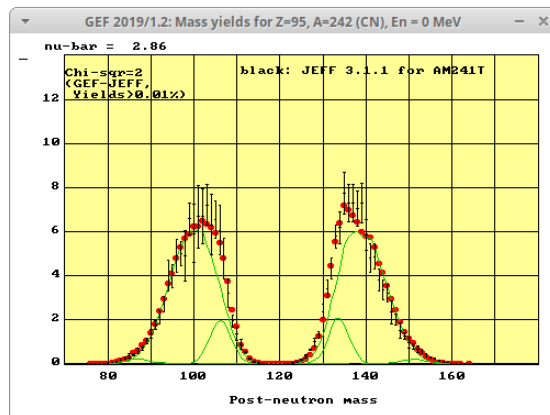


Figure 48: Mass yields of  $^{241}\text{Am}(n_{th},f)$ , linear scale, GEF result (red points) in comparison with JEFF 3.1.1 (black symbols).

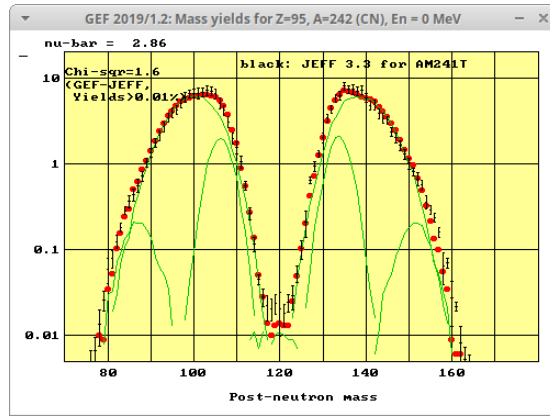


Figure 49: Mass yields of  $^{241}\text{Am}(n_{th},f)$ , logarithmic scale, GEF result (red points) in comparison with JEFF 3.3 (black symbols).

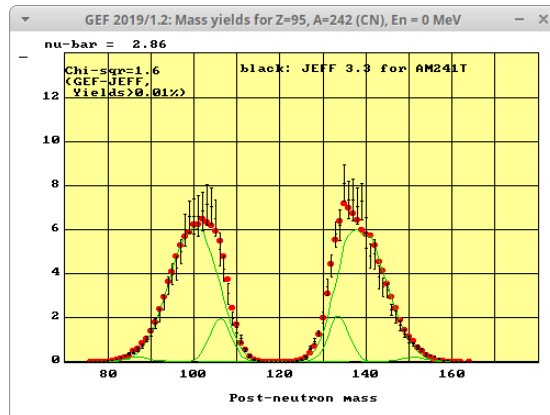


Figure 50: Mass yields of  $^{241}\text{Am}(n_{th},f)$ , linear scale, GEF result (red points) in comparison with JEFF 3.3 (black symbols).

**Mass yields in  $^{242m}\text{Am}(n_{th},f)$ :** Figures 51, 52, 53, and 54 show the comparison of the mass yields from GEF with the data from ENDF/B-VII and JEFF 3.1.1 for the system  $^{242m}\text{Am}(n_{th},f)$ . The data of the evaluations are rather well reproduced by GEF with slightly underestimated yields at symmetry.

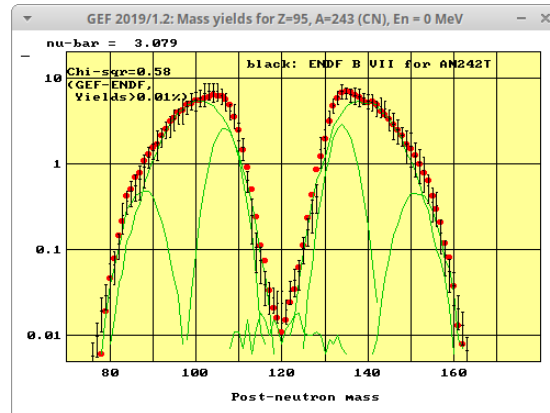


Figure 51: Mass yields of  $^{242m}\text{Am}(n_{th},f)$ , logarithmic scale, GEF result (red points) in comparison with ENDF/B-VII (black symbols).

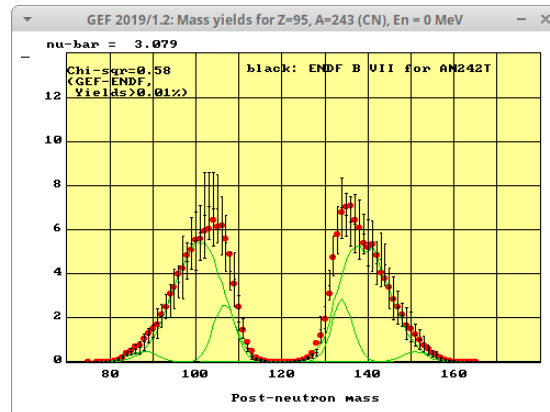


Figure 52: Mass yields of  $^{242m}\text{Am}(n_{th},f)$ , linear scale, GEF result (red points) in comparison with ENDF/B-VII (black symbols).

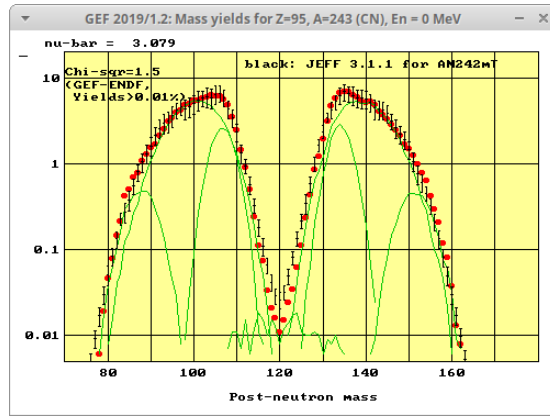


Figure 53: Mass yields of  $^{242m}\text{Am}(n_{th},f)$ , logarithmic scale, GEF result (red points) in comparison with JEFF 3.1.1 (black symbols).

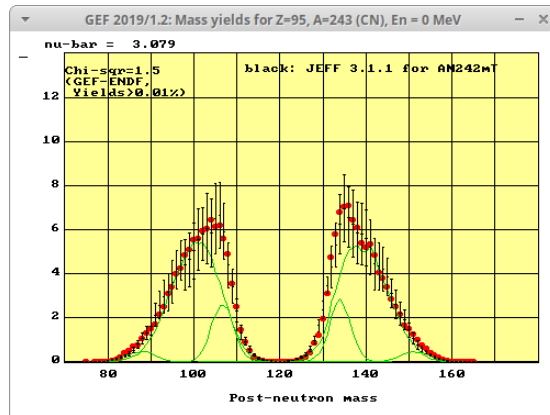


Figure 54: Mass yields of  $^{242m}\text{Am}(n_{th},f)$ , linear scale, GEF result (red points) in comparison with JEFF 3.1.1 (black symbols).

**Mass yields in  $^{243}\text{Am}(n_{th},f)$ :** Figures 55, 56, 57, and 58 show the comparison of the mass yields from GEF with the data from JEFF 3.1.1 and JEFF 3.3 for the system  $^{243}\text{Am}(n_{th},f)$ . There are discrepancies between the GEF results and JEFF 3.1.1 near symmetry and JEFF 3.3 in the outer wings, while GEF agrees well with JEFF 3.3 near symmetry and with JEFF 3.1.1 in the outer wings, which is a rather *ambiguous result that calls for clarification*.

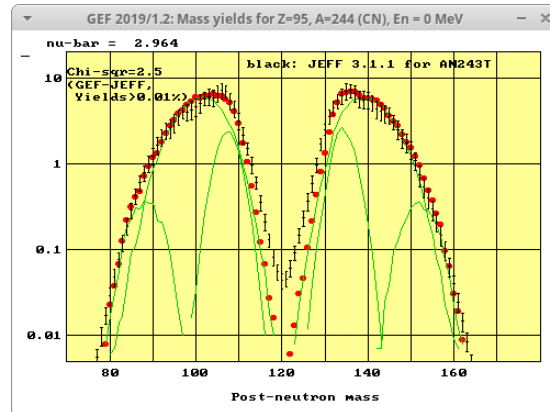


Figure 55: Mass yields of  $^{243}\text{Am}(n_{th},f)$ , logarithmic scale, GEF result (red points) in comparison with JEFF 3.1.1 (black symbols).

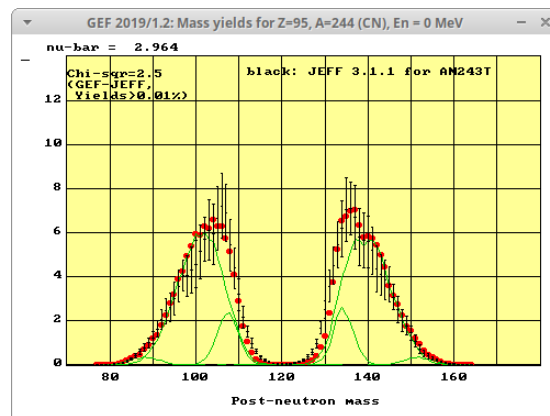


Figure 56: Mass yields of  $^{243}\text{Am}(n_{th},f)$ , linear scale, GEF result (red points) in comparison with JEFF 3.1.1 (black symbols).

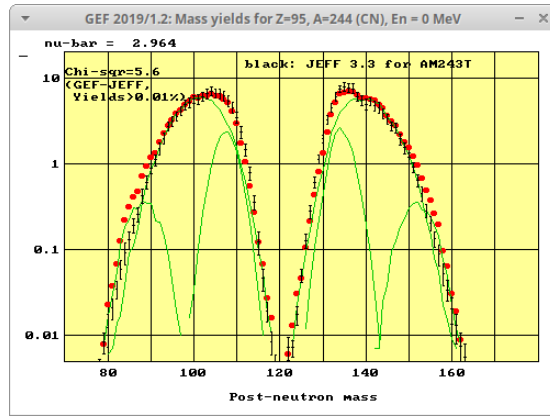


Figure 57: Mass yields of  $^{243}\text{Am}(n_{th},f)$ , logarithmic scale, GEF result (red points) in comparison with JEFF 3.3 (black symbols).

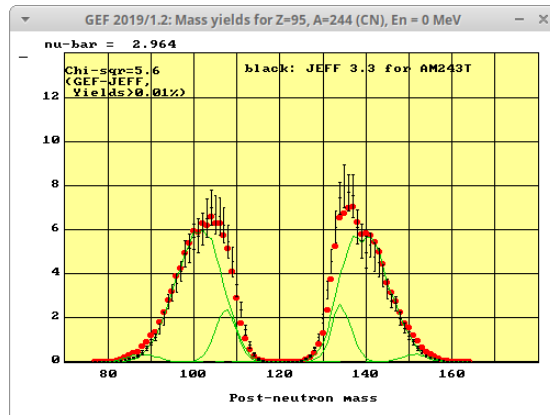


Figure 58: Mass yields of  $^{243}\text{Am}(n_{th},f)$ , linear scale, GEF result (red points) in comparison with JEFF 3.3 (black symbols).

**Mass yields in  $^{243}\text{Cm}(n_{th},f)$ :** Figures 59, 60, 61, 62, 63, and 64 show the comparison of the mass yields from GEF with the data from ENDF/B-VII, JEFF 3.1.1 and JEFF 3.3 for the system  $^{243}\text{Cm}(n_{th},f)$ . The empirical distributions are fairly well reproduced. There are some deviations, in particular around the peaks, but it is difficult to deduce a systematic trend due to the large scattering of the evaluated yields between neighbouring masses and between the different evaluations, and due to their large uncertainties.

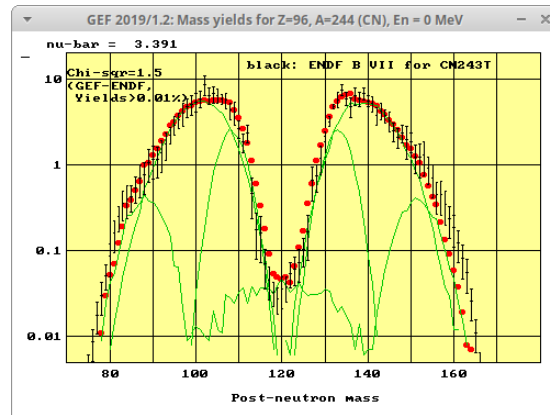


Figure 59: Mass yields of  $^{243}\text{Cm}(n_{th},f)$ , logarithmic scale, GEF result (red points) in comparison with ENDF/B-VII (black symbols).

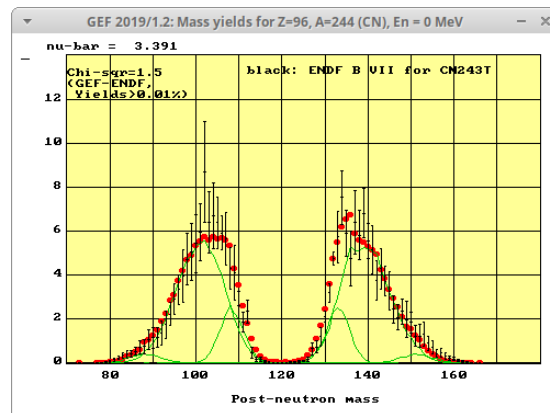


Figure 60: Mass yields of  $^{243}\text{Cm}(n_{th},f)$ , linear scale, GEF result (red points) in comparison with ENDF/B-VII (black symbols).

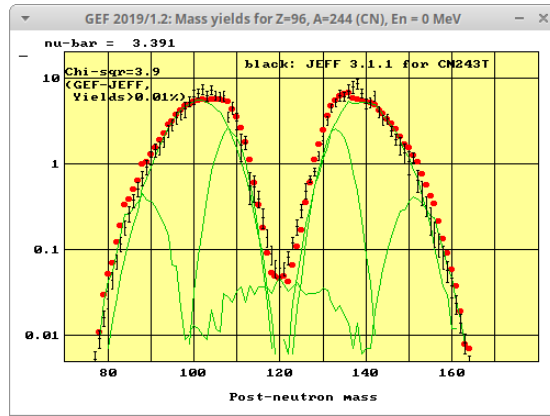


Figure 61: Mass yields of  $^{243}\text{Cm}(n_{th},f)$ , logarithmic scale, GEF result (red points) in comparison with JEFF 3.1.1 (black symbols).

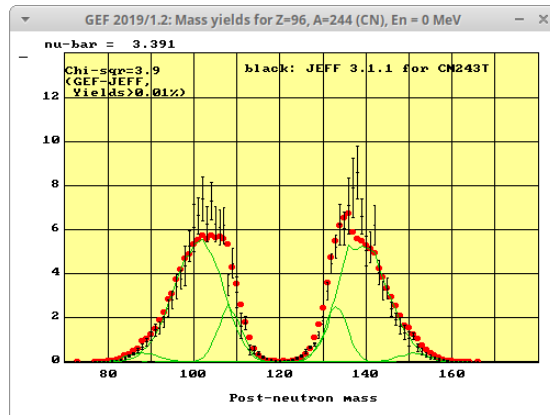


Figure 62: Mass yields of  $^{243}\text{Cm}(n_{th},f)$ , linear scale, GEF result (red points) in comparison with JEFF 3.1.1 (black symbols).

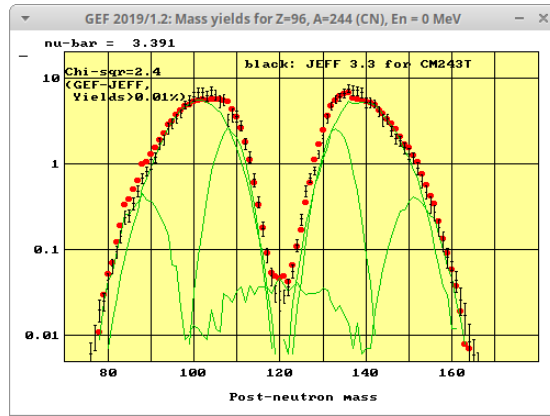


Figure 63: Mass yields of  $^{243}\text{Cm}(n_{th},f)$ , logarithmic scale, GEF result (red points) in comparison with JEFF 3.3 (black symbols).

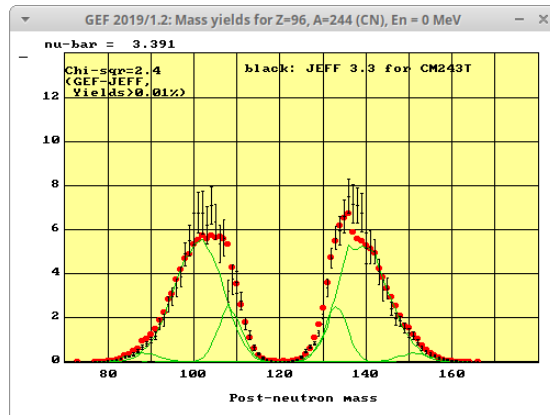


Figure 64: Mass yields of  $^{243}\text{Cm}(n_{th},f)$ , linear scale, GEF result (red points) in comparison with JEFF 3.3 (black symbols).

**Mass yields in  $^{244}\text{Cm}(n_{th},f)$ :** Figures 65, 66, 67, and 68 show the comparison of the mass yields from GEF with the data from JEFF 3.1.1 and JEFF 3.3 for the system  $^{244}\text{Cm}(n_{th},f)$ . There are large deviations between the yields from JEFF 3.1.1 and the GEF results, namely at symmetry, but rather good agreement between the yields of the more recent JEFF 3.3 evaluation and GEF.

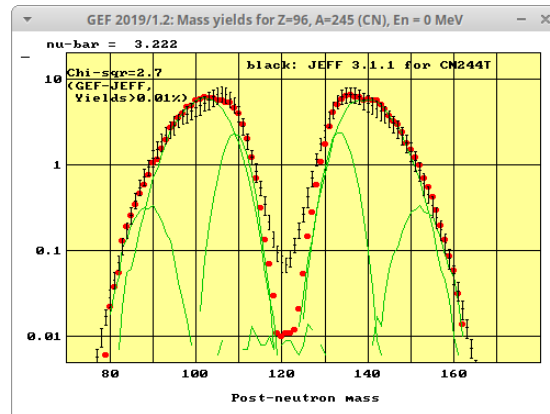


Figure 65: Mass yields of  $^{244}\text{Cm}(n_{th},f)$ , logarithmic scale, GEF result (red points) in comparison with JEFF 3.1.1 (black symbols).

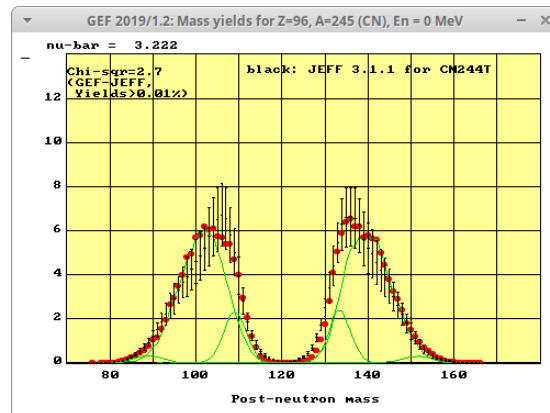


Figure 66: Mass yields of  $^{244}\text{Cm}(n_{th},f)$ , linear scale, GEF result (red points) in comparison with JEFF 3.1.1 (black symbols).

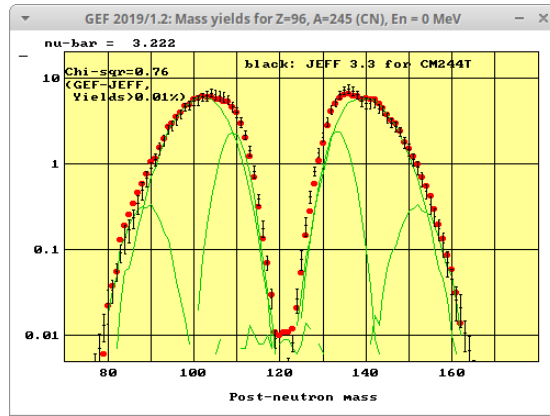


Figure 67: Mass yields of  $^{244}\text{Cm}(n_{th},f)$ , logarithmic scale, GEF result (red points) in comparison with JEFF 3.3 (black symbols).

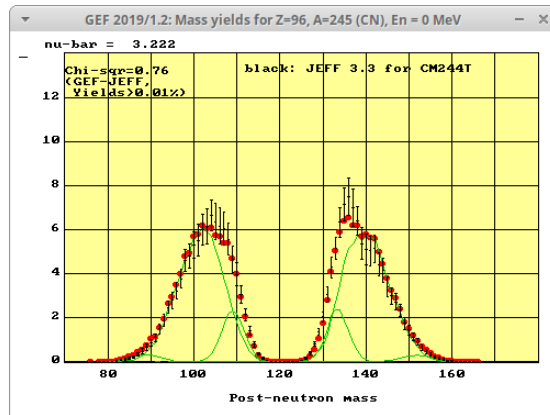


Figure 68: Mass yields of  $^{244}\text{Cm}(n_{th},f)$ , linear scale, GEF result (red points) in comparison with JEFF 3.3 (black symbols).

**Mass yields in  $^{245}\text{Cm}(n_{th},f)$ :** Figures 69, 70, 71, 72, 73, and 74 show the comparison of the mass yields from GEF with the data from ENDF/B-VII, JEFF 3.1.1 and JEFF 3.3 for the system  $^{245}\text{Cm}(n_{th},f)$ . The evaluated distributions are fairly well reproduced. There are some deviations between GEF and the one or the other evaluation, but they are not systematical. Best agreement is found between GEF and the most recent JEFF 3.3 evaluation.

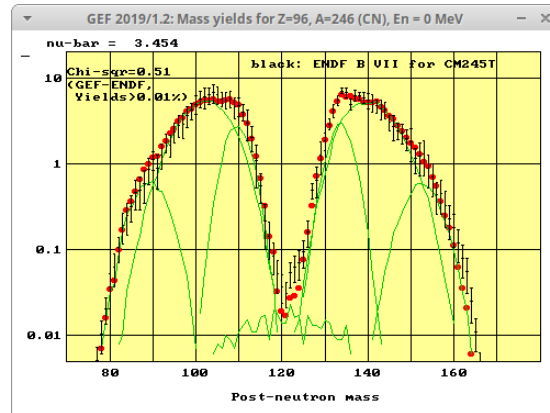


Figure 69: Mass yields of  $^{245}\text{Cm}(n_{th},f)$ , logarithmic scale, GEF result (red points) in comparison with ENDF/B-VII (black symbols).

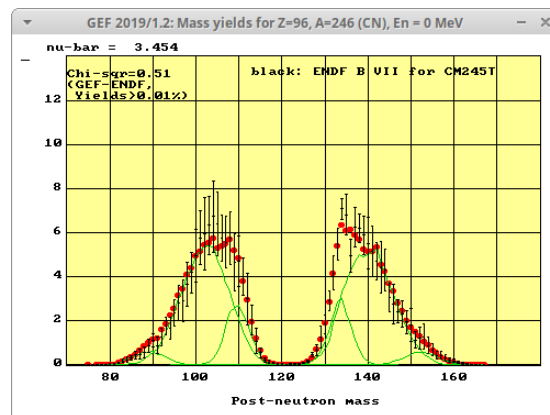


Figure 70: Mass yields of  $^{245}\text{Cm}(n_{th},f)$ , linear scale, GEF result (red points) in comparison with ENDF/B-VII (black symbols).

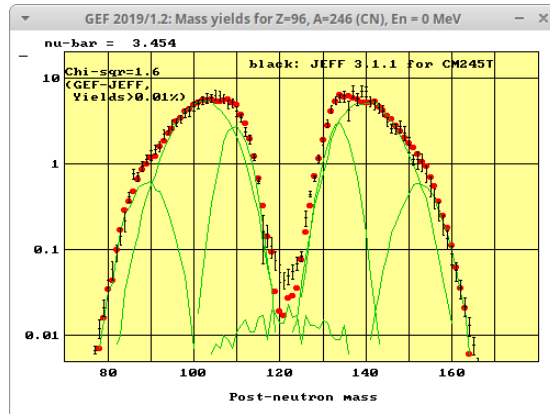


Figure 71: Mass yields of  $^{245}\text{Cm}(n_{th},f)$ , logarithmic scale, GEF result (red points) in comparison with JEFF 3.1.1 (black symbols).

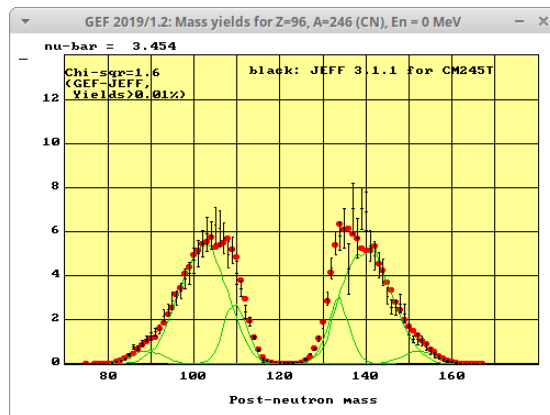


Figure 72: Mass yields of  $^{245}\text{Cm}(n_{th},f)$ , linear scale, GEF result (red points) in comparison with JEFF 3.1.1 (black symbols).

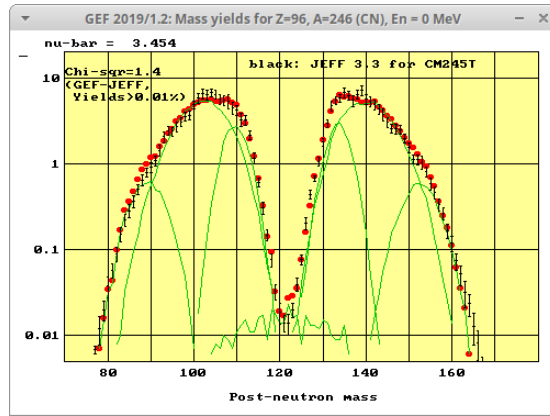


Figure 73: Mass yields of  $^{245}\text{Cm}(n_{th},f)$ , logarithmic scale, GEF result (red points) in comparison with JEFF 3.3 (black symbols).

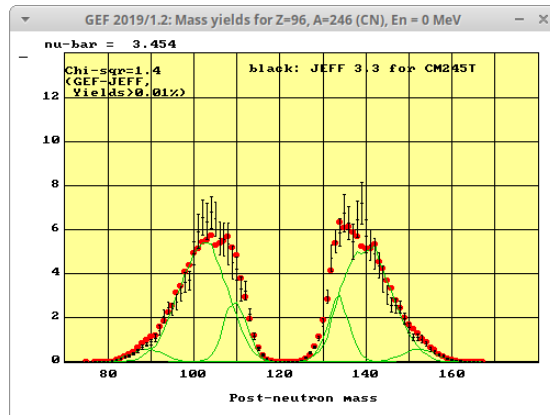


Figure 74: Mass yields of  $^{245}\text{Cm}(n_{th},f)$ , linear scale, GEF result (red points) in comparison with JEFF 3.3 (black symbols).

### 6.1.2 Treatment of energy distributions: the case of $^{238}\text{U}(\mathbf{n}_{fast},\mathbf{f})$

In several experiments, the initial excitation energy of the fissioning nucleus is not sharp. In these cases, a series of theoretical calculations with a sequence of excitation energies must be performed, and the results must be added up with the appropriate weights. A realistic description of the dependence of the fission process on the initial excitation energy is mandatory for obtaining reliable results. In the following, we present the fast-neutron-induced fission of  $^{238}\text{U}$  as an example for illustrating the procedural method.

The following data with a sharp initial excitation energy were used to benchmark the excitation-energy dependence of the fission yields in GEF: The mass yields of  $^{235}\text{U}(\mathbf{n}_{th},\mathbf{f})$ , shown above, and  $^{235}\text{U}(\mathbf{n},\mathbf{f})$  with  $E_n = 14$  MeV, shown in figures 75, 76, 77, and 78 from the ENDF/B-VII and the JEFF 3.3 evaluation, respectively, document well the variation of the fission yields from thermal energies to 14 MeV. In addition, the mass yields of  $^{238}\text{U}(\mathbf{n},\mathbf{f})$  with  $E_n = 14$  MeV, shown in figures 79, 80 and 81, and 82, were used.

One can observe a rather good agreement between the evaluated mass yields and the GEF results at fixed  $E_n$ . The growth of the symmetric channel with increasing energy, as well as the shift towards symmetry and the broadening of the asymmetric modes is well reproduced by GEF. The constraints of the theoretical framework do not allow to reproduce the data exactly, and some minor deviations can be observed: In  $^{235}\text{U}(\mathbf{n},\mathbf{f})$  with  $E_n = 14$  MeV, GEF seems to overestimate slightly the yield of the symmetric mode, and its shape is not exactly reproduced. In  $^{238}\text{U}(\mathbf{n},\mathbf{f})$  with  $E_n = 14$  MeV, however, this kind of deviation only appears with respect to ENDF/B-VII, while there is good agreement with JEFF 3.3. On the empirical side, in the mass yields of JEFF 3.3, there appear several apparently erratic deviations from the smooth behaviour of the ENDF evaluation and of GEF, which are probably not realistic.

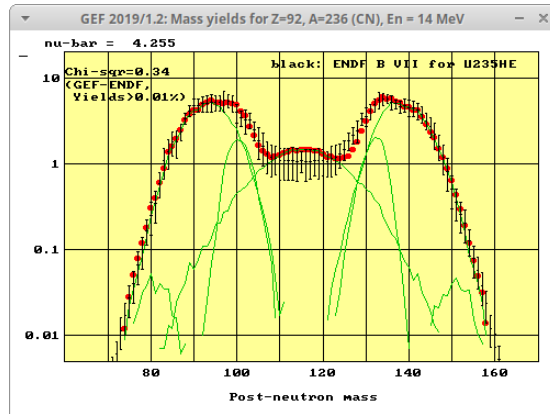


Figure 75: Mass yields of  $^{235}\text{U}(n,f)$ ,  $E_n = 14$  MeV, logarithmic scale, GEF result (red points) in comparison with ENDF/B-VII (black symbols).

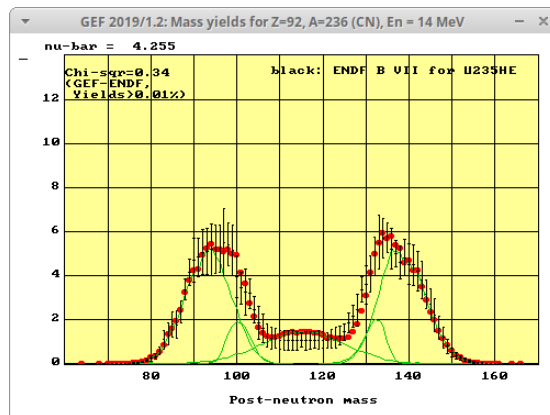


Figure 76: Mass yields of  $^{235}\text{U}(n,f)$ ,  $E_n = 14$  MeV, linear scale, GEF result (red points) in comparison with ENDF/B-VII (black symbols).

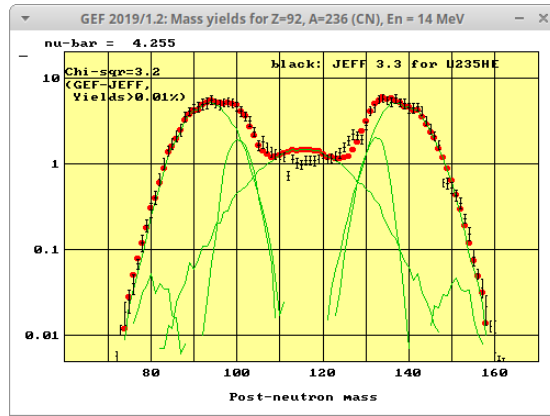


Figure 77: Mass yields of  $^{235}\text{U}(n,f)$ ,  $E_n = 14$  MeV, logarithmic scale, GEF result (red points) in comparison with JEFF 3.3 (black symbols).

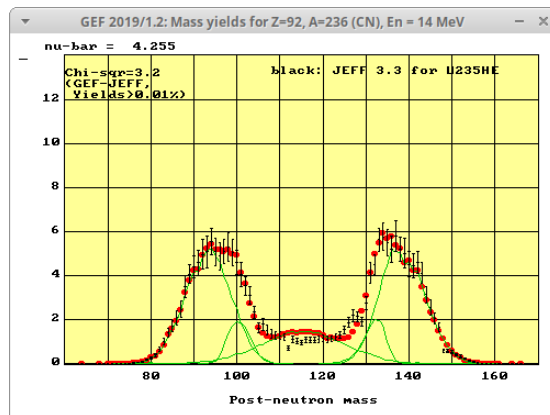


Figure 78: Mass yields of  $^{235}\text{U}(n,f)$ ,  $E_n = 14$  MeV, linear scale, GEF result (red points) in comparison with JEFF 3.3 (black symbols).

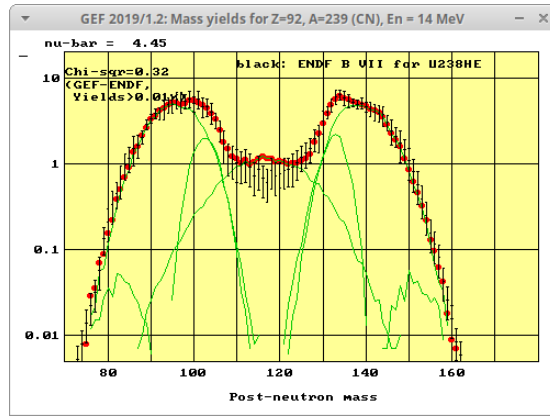


Figure 79: Mass yields of  $^{238}\text{U}(n,f)$ ,  $E_n = 14$  MeV, logarithmic scale, GEF result (red points) in comparison with ENDF/B-VII (black symbols).

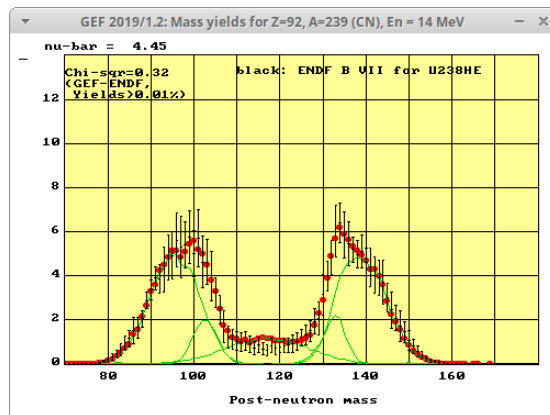


Figure 80: Mass yields of  $^{238}\text{U}(n,f)$ ,  $E_n = 14$  MeV, linear scale, GEF result (red points) in comparison with ENDF/B-VII (black symbols).

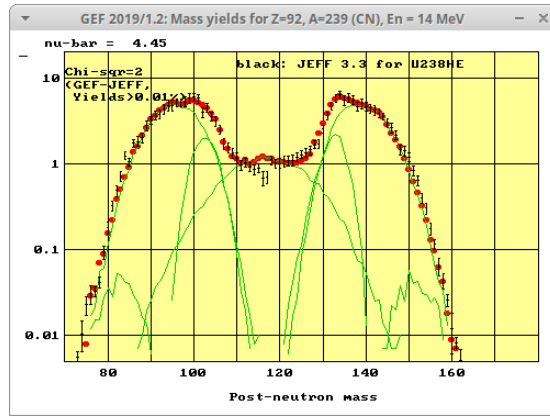


Figure 81: Mass yields of  $^{238}\text{U}(n,f)$ ,  $E_n = 14$  MeV, logarithmic scale, GEF result (red points) in comparison with JEFF 3.3 (black symbols).

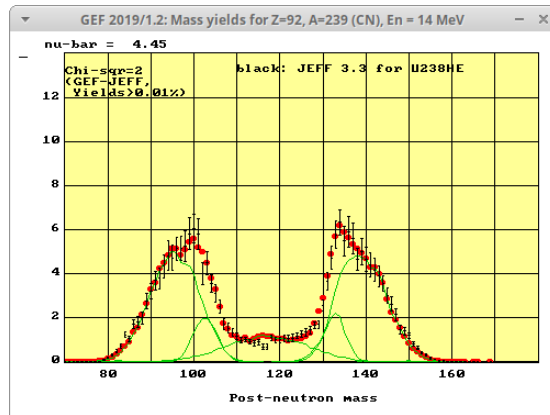


Figure 82: Mass yields of  $^{238}\text{U}(n,f)$ ,  $E_n = 14$  MeV, linear scale, GEF result (red points) in comparison with JEFF 3.3 (black symbols).

The GEF calculation of the mass yields for the system  $^{238}\text{U}(n_{fast},f)$  was performed with the distribution of initial neutron energies that lead to fission, taken from an estimation in ref. [68]. It is the spectrum of partly moderated fission neutrons, multiplied with the appropriate fission cross section of  $^{238}\text{U}$ . The corresponding initial excitation energies are shown in figure 83.

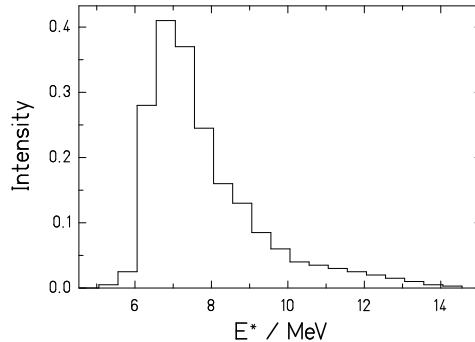


Figure 83: Initial excitation energies of the fission events in fast fission of  $^{238}\text{U}$ , rebinned from [68]. The GEF calculations were performed with a series of sharp energy values in the centres of the bins.

The result is compared with different evaluations in figures 84, 85, 86, 87, 88, and 89. The yields of the different evaluations are rather well reproduced by the GEF calculation.<sup>2</sup> There is some overestimation of the yields below 0.01 % in the extreme asymmetric wings of the distribution, which require some more detailed investigations in the future.

We would like to stress that a calculation with a sharp "mean" or "representative" value of the incident neutron energy deviates appreciably from the "exact" result, obtained with the full energy distribution.

---

<sup>2</sup>The discrepancies between the PROFIL experiment and GEF, reported in [69], do not appear any more with the latest GEF version due to the new adjustment of the model parameters in GEF Y2019/V1.2.

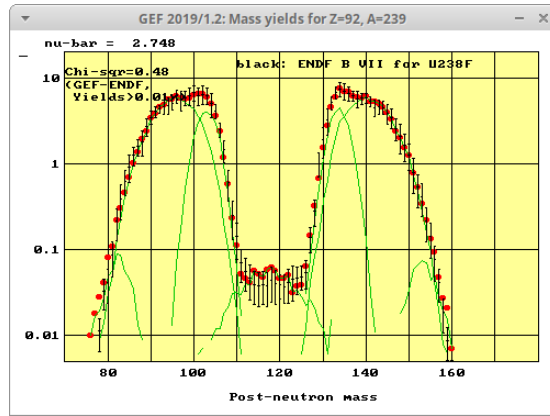


Figure 84: Mass yields of  $^{238}\text{U}(n_{fast},f)$ , logarithmic scale, GEF result (red points) in comparison with ENDF/B-VII (black symbols).

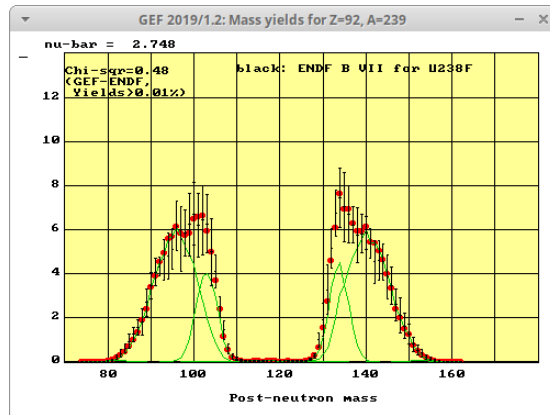


Figure 85: Mass yields of  $^{238}\text{U}(n_{fast},f)$ , linear scale, GEF result (red points) in comparison with ENDF/B-VII (black symbols).

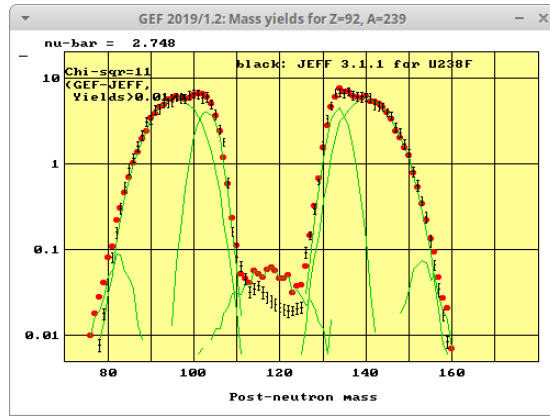


Figure 86: Mass yields of  $^{238}\text{U}(n_{fast},f)$ , logarithmic scale, GEF result (red points) in comparison with JEFF 3.1.1 (black symbols).

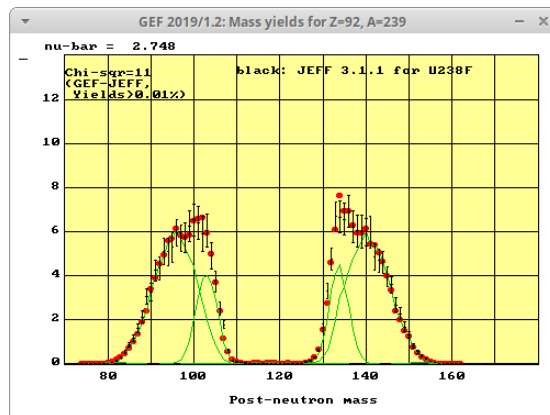


Figure 87: Mass yields of  $^{238}\text{U}(n_{fast},f)$ , linear scale, GEF result (red points) in comparison with JEFF 3.1.1 (black symbols).

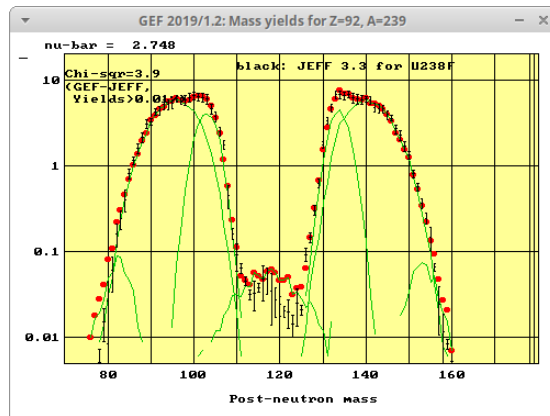


Figure 88: Mass yields of  $^{238}\text{U}(n_{fast},f)$ , logarithmic scale, GEF result (red points) in comparison with JEFF 3.3 (black symbols).

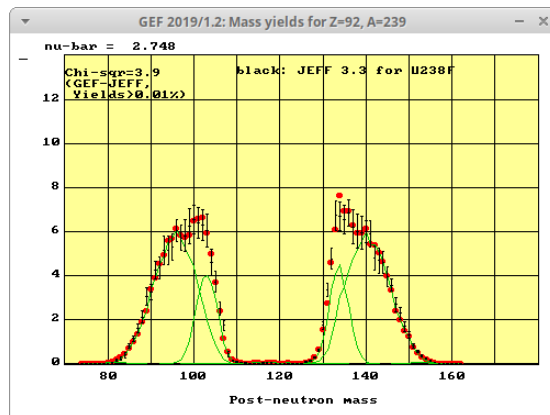


Figure 89: Mass yields of  $^{238}\text{U}(n_{fast},f)$ , linear scale, GEF result (red points) in comparison with JEFF 3.3 (black symbols).

## 6.2 Problems and proposed solutions

In this section, we compare the fission yields from different evaluations and from some LOHENGRIN experiments with the GEF results in cases of severe discrepancies. The comparisons are shown for all evaluations among the three considered in this work, which are available for the respective system.

### 6.2.1 $A=129$ yield in $^{235}\text{U}(\text{n}_{th},\text{f})$

As a semi-empirical model, GEF relies on reliable and accurate data. The inclusion of erroneous data in the adjustment of GEF parameters leads to an aberrant behaviour and to false predictions of the model. As an illustration for these difficulties, we have a closer view on the mass yield of  $A = 129$  in the thermal-neutron-induced fission of  $^{235}\text{U}$ .

Table 6: Empirical values for the  $A = 129$  yield in  $^{235}\text{U}(\text{n}_{th},\text{f})$ .

Value	Uncertainty	Reference
0.610	4.9 %	[70]
0.804	5.0 %	[71]
0.817	5.8 %	[72]
0.543	0.045	ENDF/B-VII
0.543	0.045	ENDF/B-VIII.0
0.706	0.037	JEFF 3.1.1
0.814	0.058	JEFF 3.3
0.982		GEF

Note: Selection of measured and evaluated mass yields for a case with large scattering. The GEF estimation is listed in addition.

Table 3 shows that the measured and the evaluated values scatter strongly: The highest value is larger by a factor of 1.5 than the smallest one, while the indicated uncertainties of the different values are in the order of 5 % to 10 %. In such cases, the evaluator or the developer of a semi-empirical model must make a decision, how to treat these data. For example, the uncertainty could be increased, the data could be disregarded completely, or a personal choice on the basis of additional arguments could be performed. Therefore, in an evaluation as well as in a semi-empirical model, there is inevitably a portion of subjective influence and decision. In fact, GEF is less vulnerable than an evaluation, because the inherent regularities help to identify such problematic cases, like the one illustrated in table 3: Figures 17, 18, 19, 20, 21, and 22 indicate that *the larger values given in table 3 are the more reliable ones*. In the determination of the GEF parameters, the mass yield of  $A = 129$  in  $^{235}\text{U}(\text{n}_{th},\text{f})$  was disregarded.

### 6.2.2 Mass yields in $^{227}\text{Th}(n_{th},f)$

In the figures 90 and 91, the mass yields of the system  $^{227}\text{Th}(n_{th},f)$  in ENDF/B-VII deviate strongly from the GEF results almost over the whole distribution. In particular, in view of the relatively good reproduction of the mass yields of the close system  $^{229}\text{Th}(n_{th},f)$ , the shape proposed by ENDF/B-VII seems to be erroneous. *We recommend to replace the mass yields, in particular between the asymmetric peaks, by the GEF results.* The relative yield of the symmetric fission mode, however, remains somewhat uncertain.

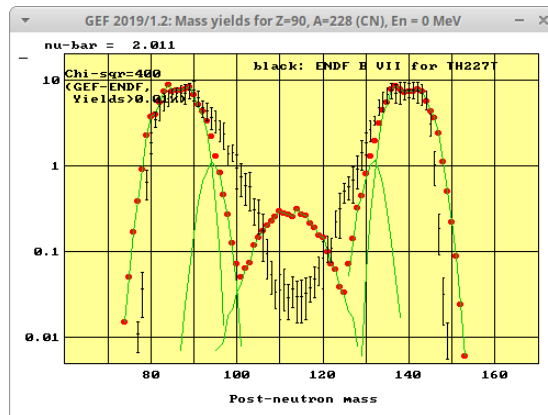


Figure 90: Mass yields of  $^{227}\text{Th}(n_{th},f)$ , logarithmic scale, GEF result (red points) in comparison with ENDF/B-VII (black symbols).

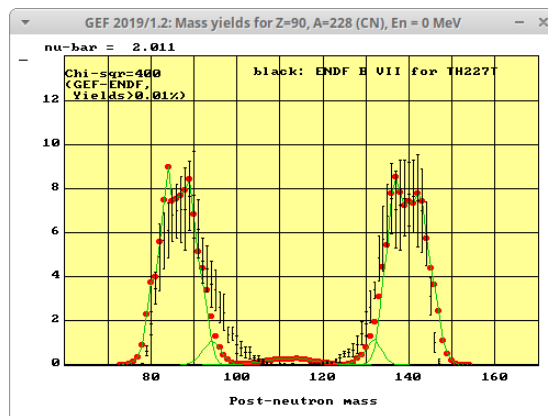


Figure 91: Mass yields of  $^{227}\text{Th}(n_{th},f)$ , linear scale, GEF result (red points) in comparison with ENDF/B-VII (black symbols).

### 6.2.3 Mass yields in $^{232}\text{U}(n_{th},f)$

In the figures 92 and 93, the mass yields of the system  $^{232}\text{U}(n_{th},f)$  in ENDF/B-VII deviate strongly from the GEF result in the wings at extreme mass asymmetry. *We recommend to replace the mass yields for  $A < 82$  and for  $A > 150$  by the GEF results.*

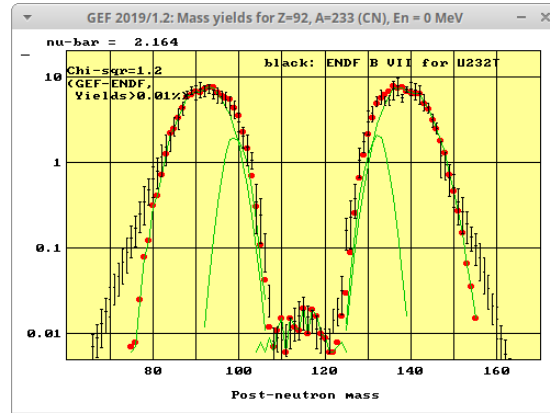


Figure 92: Mass yields of  $^{232}\text{U}(n_{th},f)$ , logarithmic scale, GEF result (red points) in comparison with ENDF/B-VII (black symbols).

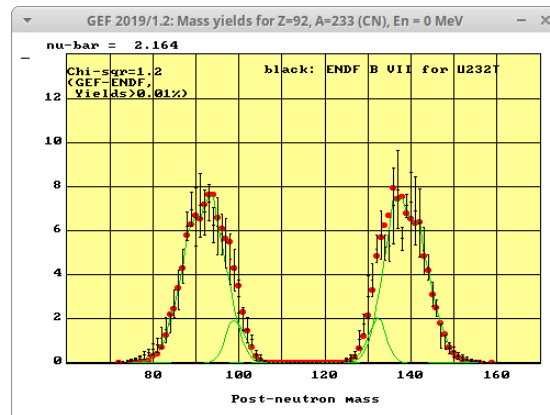


Figure 93: Mass yields of  $^{232}\text{U}(n_{th},f)$ , linear scale, GEF result (red points) in comparison with ENDF/B-VII (black symbols).

### 6.2.4 Mass yields in $^{236}\text{U}(n_{th},f)$

In figures 94 and 95, there is a clear shift in almost all the wings of the mass-yield distribution of the system  $^{236}\text{U}(n_{th},f)$ . We recommend to replace the discrepant values by the GEF results.

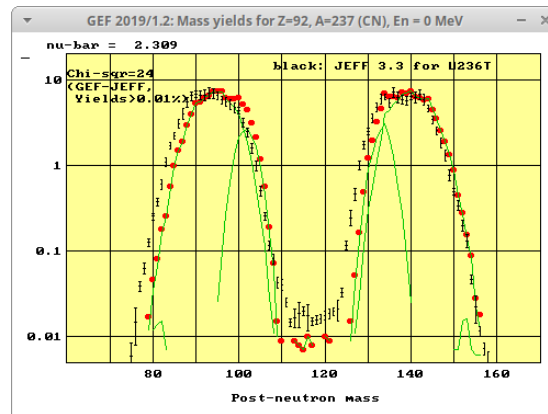


Figure 94: Mass yields of  $^{236}\text{U}(n_{th},f)$ , logarithmic scale, GEF result (red points) in comparison with JEFF 3.3 (black symbols).

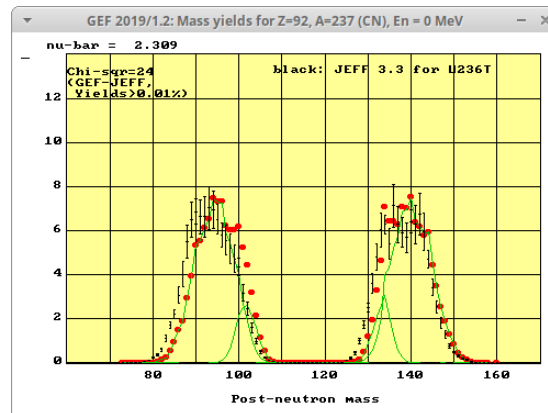


Figure 95: Mass yields of  $^{236}\text{U}(n_{th},f)$ , linear scale, GEF result (red points) in comparison with JEFF 3.3 (black symbols).

### 6.2.5 Mass yields in $^{237}\text{Np}(n_{th},f)$

In figures 96 and 97, there is a clear shift in the right wing of the light peak between GEF and ENDF/B-VII in the mass-yield distribution of the system  $^{237}\text{Np}(n_{th},f)$  and some discrepancy in the whole light peak. This problem has already been mentioned in ref. [25]. It has been attributed to a target contamination, probably of  $^{239}\text{Pu}$ . Figures 98, 99, 100, and 101 show that *this problem does not appear in the JEFF evaluations*, probably by the use of some more recent data.

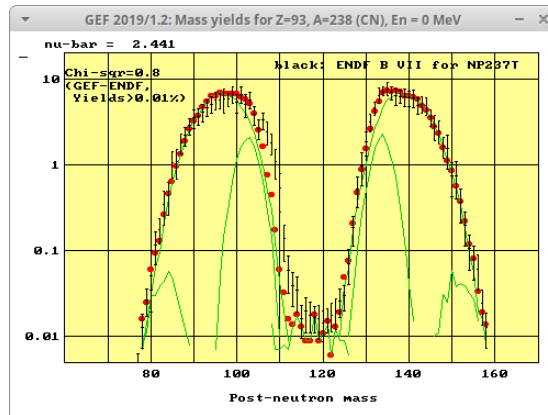


Figure 96: Mass yields of  $^{237}\text{Np}(n_{th},f)$ , logarithmic scale, GEF result (red points) in comparison with ENDF/B-VII (black symbols).

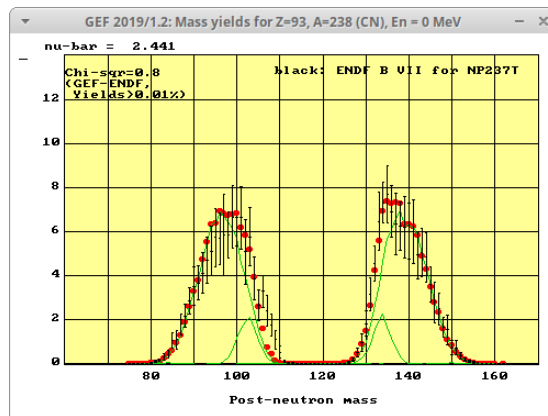


Figure 97: Mass yields of  $^{237}\text{Np}(n_{th},f)$ , linear scale, GEF result (red points) in comparison with ENDF/B-VII (black symbols).

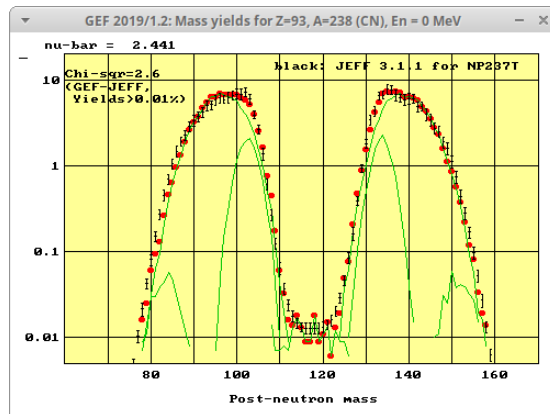


Figure 98: Mass yields of  $^{237}\text{Np}(n_{th},f)$ , logarithmic scale, GEF result (red points) in comparison with JEFF 3.1.1 (black symbols).

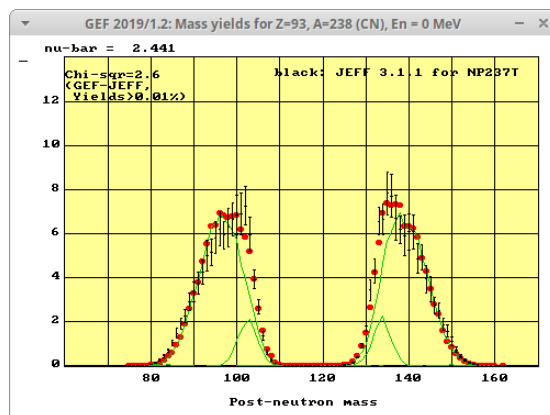


Figure 99: Mass yields of  $^{237}\text{Np}(n_{th},f)$ , linear scale, GEF result (red points) in comparison with JEFF 3.1.1 (black symbols).

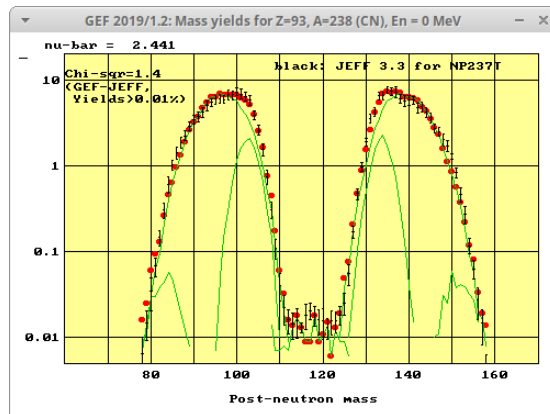


Figure 100: Mass yields of  $^{237}\text{Np}(n_{th},f)$ , logarithmic scale, GEF result (red points) in comparison with JEFF 3.3 (black symbols).

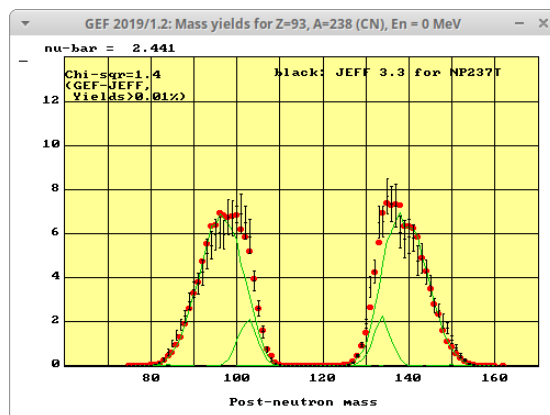


Figure 101: Mass yields of  $^{237}\text{Np}(n_{th},f)$ , linear scale, GEF result (red points) in comparison with JEFF 3.3 (black symbols).

### 6.2.6 Mass yields in $^{241}\text{Pu}(n_{th},f)$

In figures 102 and 103, 104, 105, 106, and 107 there is good agreement between the GEF results and ENDF/B-VII for mass yields of the system  $^{241}\text{Pu}(n_{th},f)$ . However, the evaluations JEFF 3.1.1 and JEFF 3.3 show strong discrepancies near symmetry and in the upper wing. *We recommend to use the ENDF compilation or the GEF results.*

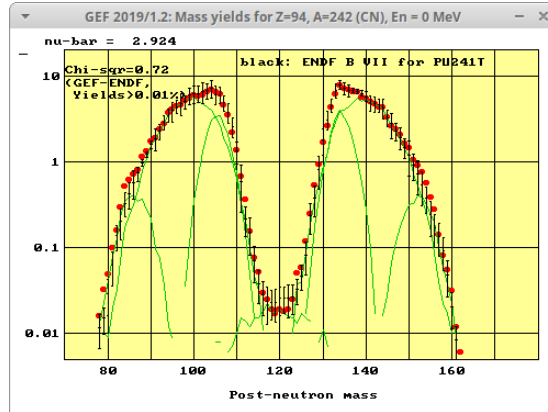


Figure 102: Mass yields of  $^{241}\text{Pu}(n_{th},f)$ , logarithmic scale, GEF result (red points) in comparison with ENDF/B-VII (black symbols).

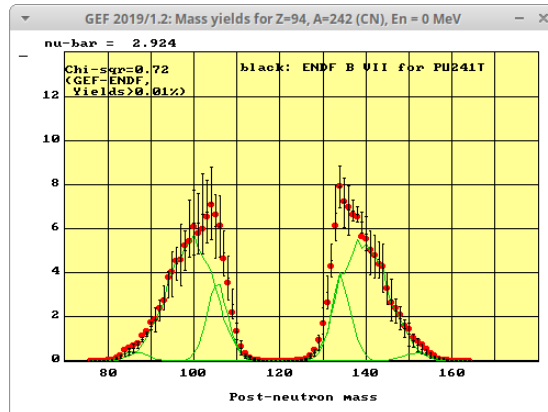


Figure 103: Mass yields of  $^{241}\text{Pu}(n_{th},f)$ , linear scale, GEF result (red points) in comparison with ENDF (black symbols).

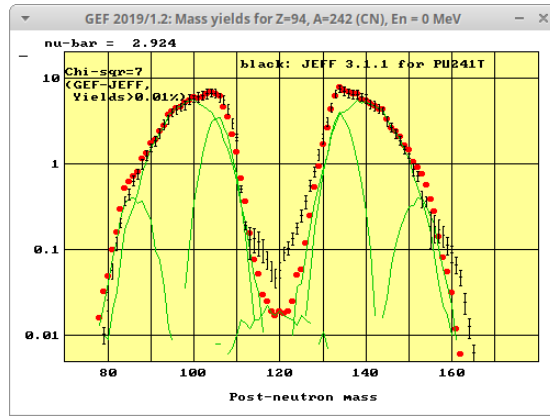


Figure 104: Mass yields of  $^{241}\text{Pu}(n_{th},f)$ , logarithmic scale, GEF result (red points) in comparison with JEFF 3.1.1 (black symbols).

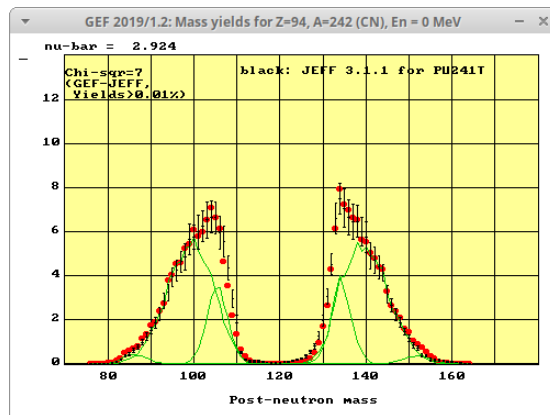


Figure 105: Mass yields of  $^{241}\text{Pu}(n_{th},f)$ , linear scale, GEF result (red points) in comparison with JEFF 3.1.1 (black symbols).

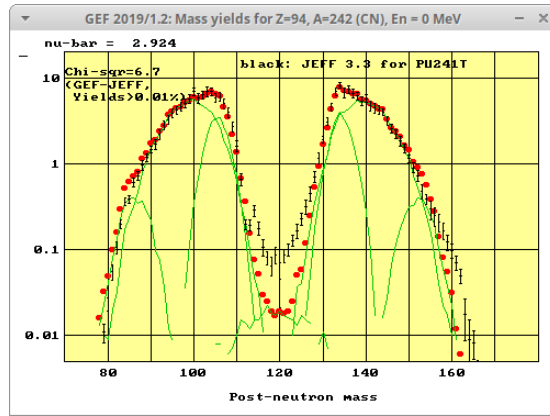


Figure 106: Mass yields of  $^{241}\text{Pu}(n_{th},f)$ , logarithmic scale, GEF result (red points) in comparison with JEFF 3.3 (black symbols).

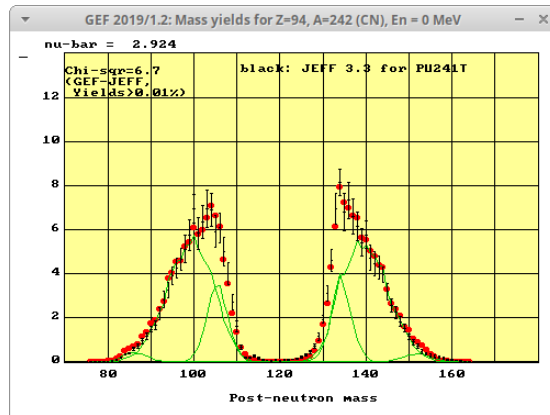


Figure 107: Mass yields of  $^{241}\text{Pu}(n_{th},f)$ , linear scale, GEF result (red points) in comparison with JEFF 3.3 (black symbols).

### 6.2.7 Mass yields in $^{251}\text{Cf}(n_{th},f)$

In figures 108 and 109, there are important discrepancies between the mass yields of ENDF/B-VII and the GEF results for the system  $^{251}\text{Cf}(n_{th},f)$ , while in figures 110 and 111, the data of the LOHENGRIN experiment [73] agree on a coarse scale quite well with the GEF results. On a finer scale, however, the LOHENGRIN data show erratic fluctuations, which are much larger than the given uncertainties. Such fluctuations are not found in the fission yields of any other system. Therefore, we attribute the fluctuations to difficulties in the experiment or in the data analysis. *We recommend to use the GEF results.*

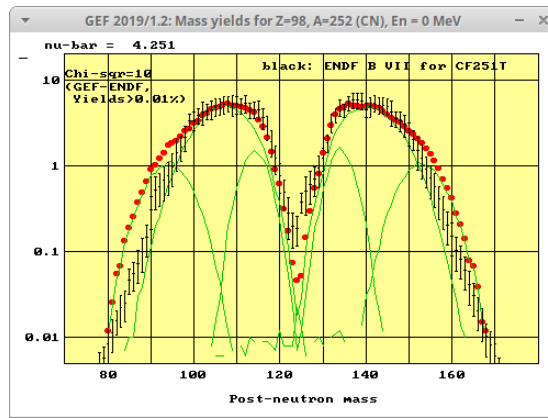


Figure 108: Mass yields of  $^{251}\text{Cf}(n_{th},f)$ , logarithmic scale, GEF result (red points) in comparison with ENDF/B-VII (black symbols).

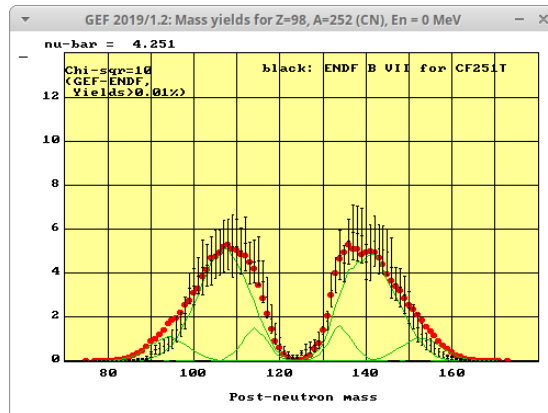


Figure 109: Mass yields of  $^{251}\text{Cf}(n_{th},f)$ , linear scale, GEF result (red points) in comparison with ENDF/B-VII (black symbols).

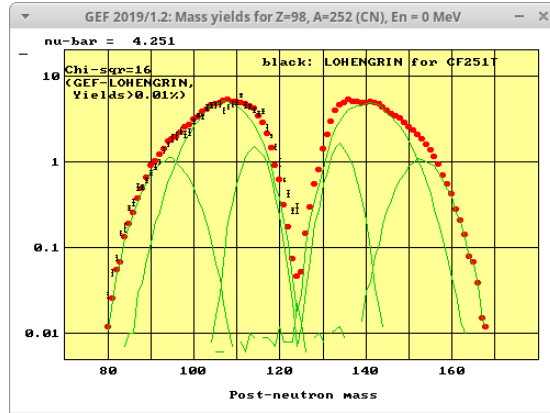


Figure 110: Mass yields of  $^{251}\text{Cf}(n_{th},f)$ , logarithmic scale, GEF result (red points) in comparison with a LOHENGRIN [73] experiment (black symbols).

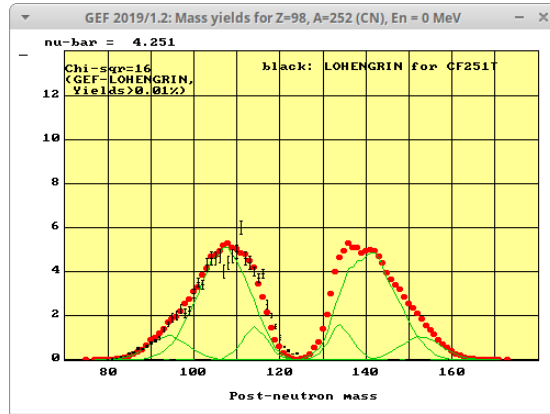


Figure 111: Mass yields of  $^{251}\text{Cf}(n_{th},f)$ , linear scale, GEF result (red points) in comparison with a LOHENGRIN [73] experiment (black symbols).

### 6.2.8 Mass yields in $^{254}\text{Es}(n_{th},f)$

In figures 112 and 113, there are strong discrepancies in the whole mass distribution between GEF and ENDF/B-VII for  $^{254}\text{Es}(n_{th},f)$ . *It is rather speculative to argue, which set of mass yields is more reliable.* It is, however, rather difficult to reconcile the fission yields from ENDF/B-VII with the inherent regularities of the GEF model.

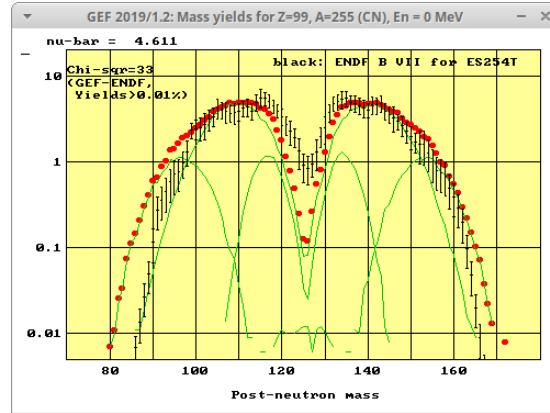


Figure 112: Mass yields of  $^{254}\text{Es}(n_{th},f)$ , logarithmic scale, GEF result (red points) in comparison with ENDF/B-VII (black symbols).

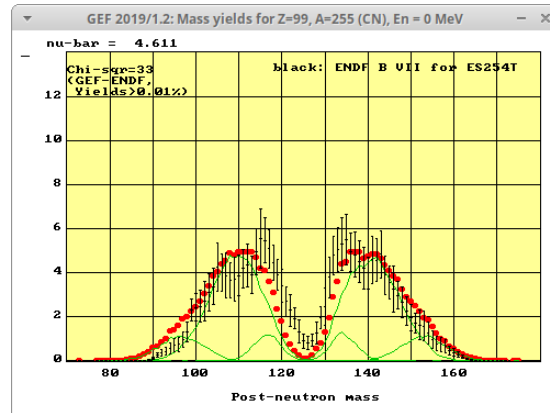


Figure 113: Mass yields of  $^{255}\text{Es}(n_{th},f)$ , linear scale, GEF result (red points) in comparison with ENDF/B-VII (black symbols).

### 6.2.9 Mass yields in $^{255}\text{Fm}(n_{th},f)$

In figures 114 and 115, there are strong discrepancies in the whole mass distribution between GEF and ENDF/B-VII for  $^{255}\text{Fm}(n_{th},f)$ . In particular, the mean value of the distribution is shifted by about 3 units. This entails a drastic difference in the mean number of prompt neutrons, where the deduced ENDF value deviates strongly from the systematics, see ref. [25]. *We recommend to replace the whole distribution by the GEF results.*

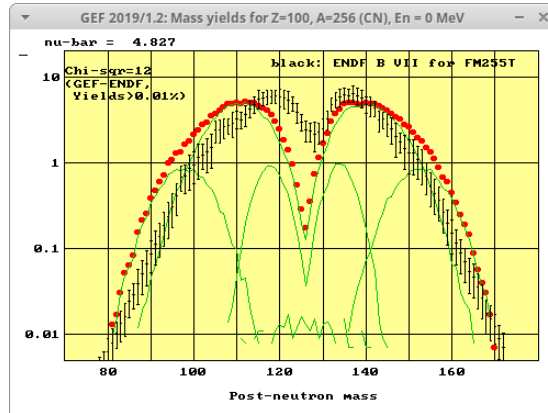


Figure 114: Mass yields of  $^{255}\text{Fm}(n_{th},f)$ , logarithmic scale, GEF result (red points) in comparison with ENDF/B-VII (black symbols).

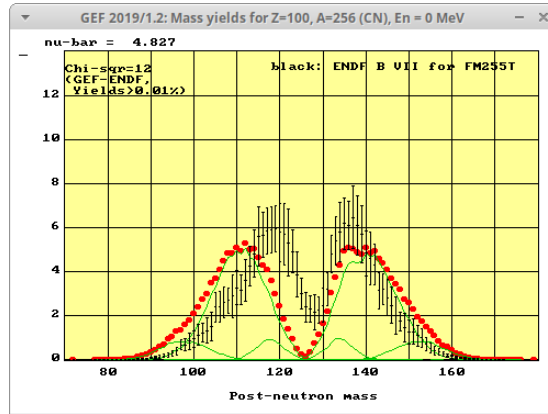


Figure 115: Mass yields of  $^{255}\text{Fm}(n_{th},f)$ , linear scale, GEF result (red points) in comparison with ENDF/B-VII (black symbols).

### 6.3 Summary

The comparative study of the preceding sections gives the following result for thermal-neutron-induced fission: In 15 cases, good or at least satisfactory agreement is obtained between the mass yields from GEF and the empirical data. In 8 cases, severe discrepancies appeared, most of them hinting to erroneous evaluations, according to our analysis. The yields at symmetry in the low-energy fission of the actinides show deviations in several systems. They pose specific difficulties to both the evaluations and the GEF code due to large experimental uncertainties in the measurement of low yields and due to the influence of weak shells on the depth of the symmetric fission valley, respectively. Most of the LOHENGRIN experiments seem to be much more accurate than the evaluations. The agreement of the mass yields with the GEF results tends to confirm the small indicated uncertainties of these experiments, except in the case of  $^{251}\text{Cf}(n_{th},f)$ . The LOHENGRIN data form a backbone for determining the parameters of GEF. However, this is not a direct adjustment. On the contrary, the compatibility of the LOHENGRIN results with the regularities and constraints of the theoretical framework of basic concepts and laws of general validity in the GEF model tends to strengthen both the LOHENGRIN data and the GEF model. Thus, the evaluations could be improved by including the LOHENGRIN data to a greater extent. The remaining deviations between empirical mass yields and GEF results reveal some deficiencies of both the evaluations and GEF, depending on the case. Local deviations for individual systems hint more to a problem in the evaluations, while general deviations for several neighbouring systems hint more to a problem in GEF. In many cases, where satisfactory agreement with the GEF result is found, but the uncertainties of the evaluations are very large, the GEF results may be included in the evaluation process and help to improve the accuracy of the evaluated mass yields. Thus, the present comparative study can be exploited to refine both the evaluations and the GEF code, leading to enhance the quality of nuclear data. This is a very important issue for the estimation of the characteristics of the anti-neutrino production, where the requirements on accuracy are extremely high.

## 7 Predictions of anti-neutrino energy spectra based on the GEF fission yields

To infer to which extent anti-neutrinos could provide a diversion signature, the characterization of the anti-neutrino source associated to different contemporary or future reactor designs and fuels is mandatory. This is to be the first step of our feasibility study and necessitates the development of simulation tools [75]. The summation method is the only predictive method that could allow such calculations. Anti-neutrino detection for reactor monitoring is thus another motivation to improve the quality of the beta decay properties and of the fission yields stored in the evaluated databases for fission products. Potential applications of anti-neutrino detectors at reactors were listed if this novel tech-

nology is approved [74]. The reactors and cases which should be addressed are: CANDU (CANadian Deuterium-Uranium) and Very High Temperature Reactors (VHTR) and among them more specifically Pebble Bed Modular Reactors (PBMR), Pressurized Water Reactors (PWR) and Boiling Water Reactors (BWR), research reactors, innovative fuel use, future reactors (other Generation IV designs than VHTR like Na-Fast Breeder Reactors (Na-FBR) or other concepts like Accelerator Driven Systems (ADS), ...). The two first designs, CANDU and PBMR are on-load reactors for which it is not necessary to stop the operation of the core to refuel it. For these reactors, an anti-neutrino detector placed outside the containment walls at a moderate distance could offer a form of bulk accountancy of the fuel content of the core. These designs imply thermal and fast fissions for various fuels. The nuclear data of the fission yields are still scarce for the fuels departing from the most standard ones in use in nowadays power plants, and the GEF model can provide a mean to get reliable predictions with uncertainties.

## 7.1 Anti-neutrino energy spectra

The anti-neutrino energy spectra for the systems listed in the first part of this article have been computed using the GEF cumulative fission yields combined with the nuclear data of the beta decay properties of the fission products described above. They are shown in Fig. 116.

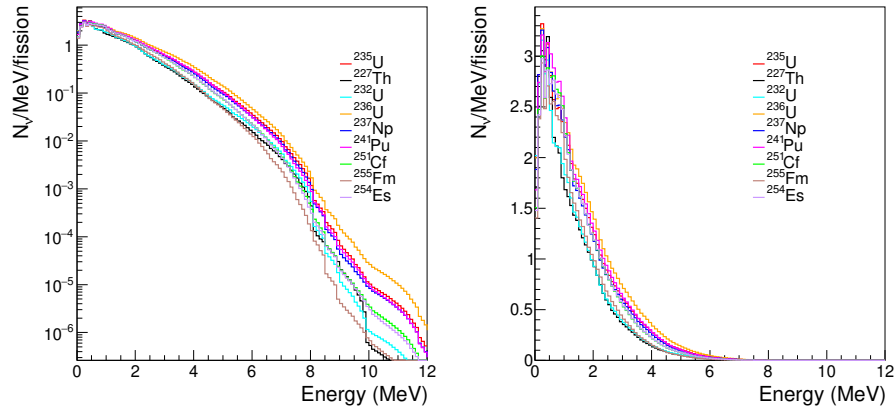


Figure 116: Calculated antineutrino spectra from GEF combined with the selection of decay data of [22] for different systems in logarithmic (left) and linear (right) scale.

## 7.2 Sensitivity to the fissioning system

The possible application of anti-neutrino spectroscopy for reactor monitoring depends essentially on the sensitivity of the anti-neutrino energy spectrum to the fissioning system. A first glance on this sensitivity can be obtained by accumulating the Q values of the consecutive beta decays of the fission fragments with their respective appearances. This signature has the advantage not to be influenced by the branchings of the beta decay to excited levels. This could introduce a bias, because the experimental knowledge on these branchings is systematically less detailed for the more neutron-rich nuclei.

Figure 117 shows this accumulated distribution of Q-values for the following systems:  $^{235}\text{U}(n_{th},f)$ ,  $^{238}\text{U}(n_{fast},f)$ ,  $^{239}\text{Pu}(n_{th},f)$ , and  $^{241}\text{Pu}(n_{th},f)$ . Obviously, there is a systematic and rather important increase of the multiplicity, in particular at higher energies, with increasing  $A/Z$  of the fissioning system. Because the relative enhancement is energy dependent, the shape of the anti-neutrino energy spectrum is sensitive to the relative contributions of the different fissioning systems. Combining this information with the expected uncertainty of the measured anti-neutrino energy spectrum will provide a good estimation of the sensitivity of anti-neutrino spectroscopy for reactor monitoring in specific cases.

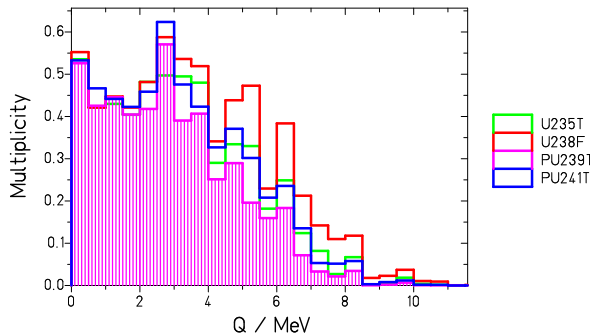


Figure 117: Spectrum of the Q values of the consecutive beta decays of the fission fragments for the systems  $^{235}\text{U}(n_{th},f)$ ,  $^{238}\text{U}(n_{fast},f)$ ,  $^{239}\text{Pu}(n_{th},f)$ , and  $^{241}\text{Pu}(n_{th},f)$ , calculated with the GEF code. For clarity, the spectrum is shown with a coarse binning of 500 keV.

## 8 Conclusion

The calculation of the anti-neutrino production in fission reactors is presently one of the most demanding applications of nuclear data due to the high required accuracy. This is true for both solving problems of neutrino physics and applying neutrino spectroscopy for reactor monitoring. In the present work, it was shown that the presently reached quality of related nuclear data, in particular

of the fission yields, can appreciably be improved by exploiting and combining different approaches: traditional radio-chemical experiments, kinematical experiments and suitable theoretical models. For the first time, a careful analysis and a systematic comparison between data from different sources and evaluations and with GEF have been performed to sort out the more reliable and the less trustworthy values, thus assisting the evaluation process.

Examples were shown of how erroneous data in different evaluations, up to very recent ones, can be detected and rather credible estimations of un-measured values can be performed. In a number of cases, personal recommendations were given to replace apparently erroneous data by more realistic estimations.

As a result of this work, the level of agreement attained on the anti-neutrino energy spectra computed with the new GEF fission yields or with the JEFF evaluated fission yields has been remarkably improved in the case of the four main fissioning systems in actual reactors.

A systematics of calculated intensities and beta Q values of all fission fragments for the four most important fissioning systems, contributing to the anti-neutrino production in a fission reactor, reveals some prevailing characteristics of the underlying fission and radioactive-decay processes. These are crucial for estimating the sensitivity of a possible application of anti-neutrino production to reactor monitoring. Predictions of anti-neutrino energy spectra based on the GEF fission yields combined with the most recent decay data sets from [22] are provided for a list of fissioning systems which could be used in the frame of such sensitivity studies.

By extending the GEF calculations, presented in this work, with explicit calculations of the beta-decay energies, including error propagation and correlations, one obtains a powerful tool for identifying the specific problems and limitations of the summation method that determine the quality that can presently be reached. This can also be used for establishing a list of most urgent improvements of the quality of underlying nuclear data.

## Acknowledgement

This work was supported by SUBATECH, Nantes, by financing several research visits in 2018. K.-H. S. thanks the SUBATECH for warm hospitality.

## References

- [1] Bedrich Roskovec, arXiv 1812.03206 (2018).
- [2] F. Reines, C.L. Cowan, Jr., *Nature* **178** (1956) 446.
- [3] Y. Abe *et al.*, *Phys. Rev. Lett.* **108** (2012) 131801.
- [4] F. P. An *et al.*, *Phys. Rev. Lett.* **108** (2012) 171803.
- [5] J. K. Ahn *et al.*, *Phys. Rev. Lett.* **108** (2012) 191802.

- [6] L.A. Mikaelian, 1977, Proc. Int. Conf. Neutrino-77, v.2, p.383.
- [7] K. Schreckenbach *et al.*, Phys. Lett. **99B** (1981) 251.
- [8] K. Schreckenbach *et al.*, Phys. Lett. **160B** (1985) 325.
- [9] F. von Feilitzsch, A. A. Hahn, K. Schreckenbach, Phys. Lett. **118B** (1982) 162.
- [10] A. A. Hahn *et al.*, Phys. Lett. **B 218** (1989) 365.
- [11] T. A. Mueller *et al.*, Phys. Rev. **C 83** (2011) 054615.
- [12] P. Huber, Phys. Rev. **C84** (2011) 024617.
- [13] F. P. An *et al.*, Chinese Phys. **C 41** (2017) 013002.
- [14] G. Mention *et al.*, Phys. Rev. **D 83** (2011) 073006.
- [15] K. N. Abazajian *et al.*, <http://arxiv.org/abs/1204.5379>.
- [16] A. C. Hayes, J.L. Friar, G.T. Garvey, G.Jungman, G. Jonkmans, Phys. Rev. Lett. **112** (2014) 202501.
- [17] D. L. Fang, B. A. Brown, Phys. Rev. **C 91** (2015) 025503.
- [18] L. Hayen *et al.*, Phys. Rev. **C 99** (2019) 031301.
- [19] M. Fallot *et al.*, Phys. Rev. Lett. **109** (2012) 202504.
- [20] A. A. Zakari-Issoufou *et al.*, Phys. Rev. Lett. **115** (2015) 102503.
- [21] A. A. Sonzogni, T. D. Johnson, E. A. McCutchan, Phys. Rev. **C 91** (2015) 011301(R).
- [22] M. Estienne *et al.*, Phys. Rev. Lett. **123** (2019) 022502, <http://arxiv.org/abs/1904.09358>
- [23] A. C. Hayes *et al.*, Phys. Rev. **D 92** (2015) 033015.
- [24] Ma Xubo, Yang le, Zhan Liang, An Fengpeng, Cao Jun, arXiv 1807.09265 (2018).
- [25] K.-H. Schmidt, B. Jurado, C. Amouroux, C. Schmitt, Nucl. Data Sheets **131** (2016) 107.
- [26] K.-H. Schmidt, B. Jurado, Rep. Progr. Phys. **81** (2018) 106301.
- [27] Ch. Schmitt, K.-H. Schmidt, B. Jurado, Phys. Rev. **C 98** (2018) 044605.
- [28] W. D. Myers, W. J. Swiatecki, Nucl. Phys. **A 601** (1996) 14.
- [29] U. Mosel, H. W. Schmitt, Nucl. Phys. **A 165** (1971) 73.

- [30] K.-H. Schmidt, A. Kelic, M. V. Ricciardi, *Europh. Lett.* **83** (2008) 32001.
- [31] B. D. Wilkins, E. P. Steinberg, R. R. Chasman, *Phys. Rev. C* **14** (1976) 1832.
- [32] H. Nifenecker, *J. Physique Lett.* **41** (1980) 47.
- [33] K.-H. Schmidt, B. Jurado, *Phys. Rev. C* **86** (2012) 044322.
- [34] K.-H. Schmidt, B. Jurado, *Phys. Rev. Lett.* **104** (2010) 212501.
- [35] K.-H. Schmidt, B. Jurado, *Phys. Rev. C* **83** (2011) 014607.
- [36] K.-H. Schmidt, B. Jurado, *Phys. Rev. C* **83** (2011) 061601.
- [37] B. Jurado, K.-H. Schmidt, *J. Phys. G: Nucl. Part. Phys.* **42** (2015) 055101.
- [38] H. J. Specht, *Physica Scripta* **10A** (1974) 21.
- [39] H. J. Specht, *Rev. Mod. Phys.* **46** (1974) 773.
- [40] R. W. King, J. F. Perkins, *Phys. Rev.* **112** (1958) 963.
- [41] F. T. Avignone *et al.*, *Phys. Rev.* **170** (1968) 931.
- [42] P. Vogel, G. K. Schenter, F. M. Mann, R. E. Schenter, *Phys. Rev. C* **24** (1981) 1543.
- [43] O. Tengblad *et al.*, *Nuclear Physics A* **503** (1989) 136. G. Rudstam *et al.*, *Atomic Data and Nucl. Data Tables* **45** (1990) 239.
- [44] J. C. Hardy *et al.*, *Phys. Lett. B* **71** (1977) 307.
- [45] B. Rubio, W. Gelletly, *Romanian Reports in Physics*, **59** (2007) 635.
- [46] A. Algora *et al.*, *Phys. Rev. Lett.* **105** (2010) 202501.
- [47] E. Valencia *et al.*, *Phys. Rev. C* **95** (2017) 024320.
- [48] S. Rice *et al.*, *Phys. Rev. C* **96** (2017) 014320.
- [49] V. Guadilla *et al.*, *Phys. Rev. Lett.* **122** (2019) 042502.
- [50] P. Dimitriou and A. L. Nichols, IAEA report INDC(NDS)-0676, Feb. 2015, IAEA, Vienna, Austria.
- [51] A. N. Andreyev, K. Nishio, K.-H. Schmidt, *Rep. Progr. Phys.* **81** (2018) 016301.
- [52] J. Laurec *et al.*, *Nucl. Data Sheets* **111** (2010) 2965.
- [53] A. C. Wahl, *J. Radioanalytical Chem.* **55** (1980) 111.
- [54] A. C. Wahl, "Systematics of Fission-Product Yields", LA-13928, (2002).

- [55] E. Moll *et al.*, Nucl. Instrum. Methods **123** (1975) 615.
- [56] U. Köster *et al.*, Nucl. Instrum. Methods **A 613** (2010) 363.
- [57] H. Wohlfarth *et al.*, Z. Phys. **A 287** (1978) 153.
- [58] K.-H. Schmidt *et al.*, Nucl. Phys. **A 665** (2000) 221.
- [59] M. Caamano *et al.*, Phys. Rev. **C 88** (2013) 024605.
- [60] G. Boutoux *et al.*, Physics Procedia **47** (2013) 166.
- [61] J. P. Bocquet *et al.*, Z. Phys. **A 335** (1990) 41.
- [62] U. Quade *et al.*, Nucl. Phys. **A 487** (1988) 1.
- [63] W. Lang *et al.*, Nucl. Phys. **A 345** (1980) 34.
- [64] J. L. Sida *et al.*, Nucl. Phys. **A 502** (1989) 233c-242c.
- [65] G. Martinez *et al.*, Nucl. Phys. **A 515** (1990) 433.
- [66] I. Tsekhanovich *et al.*, Nucl. Phys. **A 688** (2001) 633.
- [67] C. Schmitt *et al.* Nucl. Phys. **A 430** (1984) 21.
- [68] Kilian Kern, Maarten Becker, Cornelis Broeders, PHYSOR Advances in Reactor Physics (2012) 1.
- [69] E. Privas *et al.*, EPJ Nuclear Sci. Technol. **2** (2016) 32.
- [70] M. M. Fowler, A. C. Wahl, J. Inorganic Nucl. Chem. **36** (1974) 1201.
- [71] G. Diiorio, B. W. Wehring, Nucl. Instrum. Methods B **147** (1977) 487.
- [72] H. Thierens *et al.*, Nucl. Instrum. Methods **134** (1976) 299.
- [73] E. Birgersson *et al.*, Nucl. Phys. A **791** (2007) 1.
- [74] IAEA Report SG-EQGNRL-RP-0002 (2012) and IAEA Report STR-361, (2009).
- [75] S. Cormon *et al.*, Nucl. Data Sheets **120** (2014) 141.
- [76] Yeongduk Kim, Journal of Physics: Conf. Series **888** (2017) 012010.